



HAL
open science

Pore pressure pulse migration in microcracked andesite recorded with fibre optic sensors

A. Nicolas, G Blöcher, C Kluge, Z Li, H Hofmann, L. Pei, H Milsch, J. Fortin,
Y. Guéguen

► **To cite this version:**

A. Nicolas, G Blöcher, C Kluge, Z Li, H Hofmann, et al.. Pore pressure pulse migration in microcracked andesite recorded with fibre optic sensors. *Geomechanics for Energy and the Environment*, 2020, 10.1016/j.gete.2020.100183 . hal-02567554

HAL Id: hal-02567554

<https://hal.science/hal-02567554>

Submitted on 14 May 2020

HAL is a multi-disciplinary open access archive for the deposit and dissemination of scientific research documents, whether they are published or not. The documents may come from teaching and research institutions in France or abroad, or from public or private research centers.

L'archive ouverte pluridisciplinaire **HAL**, est destinée au dépôt et à la diffusion de documents scientifiques de niveau recherche, publiés ou non, émanant des établissements d'enseignement et de recherche français ou étrangers, des laboratoires publics ou privés.

**1 Pore pressure pulse migration in microcracked
2 andesite recorded with fibre optic sensors**

A. Nicolas¹, G. Blöcher², C. Kluge², Z. Li¹, H. Hofmann², L. Pei^{2,3}, H.

Milsch², J. Fortin¹, Y. Guéguen¹

Corresponding author: A. Nicolas, Laboratoire de Géologie, Ecole Normale Supérieure, Paris, France. (nicolas@geologie.ens.fr)

¹Laboratoire de Géologie, Ecole Normale Supérieure - PSL Research University -, CNRS, UMR 8538, Paris, France.

²Helmholtz Centre Potsdam - GFZ German Research Centre for Geosciences, Telegrafenberg, 14473 Potsdam, Germany

³Chinese Academy of Sciences, Institute of Rock and Soil Mechanics, Wuhan, China

Abstract. Pore pressure has a major influence on the effective stress and thus on the mechanical behaviour of rocks. In this study, we focus on the hydro-mechanical behaviour of a low porosity andesitic rock heat-treated to 930°C to induce thermal cracks and increase the permeability of the samples. First, we show that permeability decreases from $8 \times 10^{-16} \text{m}^2$ to $1.5 \times 10^{-17} \text{m}^2$ with a confining pressure (P_c) increase from 2 MPa to 40 MPa (pore pressure being approximately 0.2 MPa). Then, we used fibre optic pressure sensors to monitor pore pressure diffusion at three points along the sample during the propagation of a pore pressure pulse under hydrostatic ($P_c=40$ MPa) and triaxial stresses ($P_c=40$ MPa, differential stress of 356 MPa). When the pore pressure pulse was applied, the fibre optic sensors showed a sudden pore pressure increase one after the other as a function of their location along the sample. Pore pressure increase downstream was very smooth under hydrostatic stress and almost zero after the duration of the experiment (50 minutes) under triaxial stresses. This lack of downstream pore pressure increase under triaxial stresses is due to the fact that a differential stress of 356 MPa decreased permeability from approximately 10^{-17}m^2 to approximately 10^{-19}m^2 . Finally, the pore pressure diffusion process was modelled considering a uniform spatial distribution of permeability in the andesite sample and the dead volume attached at the downstream side.

1. Introduction

23 Rock permeability and its evolution with changes of external stress and pore pressure is
24 of interest for industrial purposes such as petroleum and geothermal reservoir engineering,
25 radioactive waste management, CO₂ sequestration and for the understanding of natural
26 hazards such as earthquakes. Human activities can lead to increases in effective stress
27 because of pore pressure decrease, for example during hydrocarbon or geothermal fluid
28 extraction [e.g. *Segall and Fitzgerald*, 1998]. Increases of effective pressure (external stress
29 minus pore pressure) can lead to a decrease of permeability [e.g. *David et al.*, 1994; *Miller*,
30 2002; *Bemer and Lombard*, 2010] causing a reduction of the production rate in geo-fluids
31 exploitation. In geothermal fields situated in andesitic areas, permeability distribution
32 can vary over a wide range of values and fault zones usually control fluids pathways [e.g.
33 *Brehme et al.*, 2016a, b]. As geothermal energy is currently developed [e.g. *Tester et al.*,
34 2006; *Zimmermann and Reinicke*, 2010], it is necessary to understand the links between
35 fluid pressure, mechanical behaviour and possible seismicity at all scales [e.g. *Shapiro and*
36 *Dinske*, 2009a, b; *Zang et al.*, 2014; *Johann et al.*, 2016; *Katayama et al.*, 2018; *Chanard*
37 *et al.*, 2019]. In enhanced geothermal systems, stimulation significantly increases pore
38 pressure [*Häring et al.*, 2008], leading to a reduction of effective stress. Reduced effective
39 stress generates new fluid path ways, thus increasing production efficiency [*Zimmermann*
40 *et al.*, 2009] but it may also induce slip on pre-stressed discontinuities [e.g. *Majer et al.*,
41 2007; *Deichmann and Giardini*, 2009; *Terakawa et al.*, 2012].

42 In the laboratory, it has been shown that even in the elastic domain, the effective stress
43 law for the permeability is not straightforward [e.g. *Ghabezloo et al.*, 2009; *Braun et al.*,
44 2018] but is of major importance for prediction of permeability evolution in stressed
45 geo-materials [e.g. *Shapiro et al.*, 1997, 2003]. At stresses beyond the elastic domain of

46 the rock, crack propagation or nucleation, and plasticity add complexities. Depending
47 on the failure mode of the rock considered, permeability can either increase or decrease
48 with increasing damage [e.g. *Zhu and Wong, 1997*] because rock deformation can occur
49 with compaction or dilatancy of the porous medium. Brittle deformation can lead to
50 dramatic changes of permeability because of changes of crack density and connectivity
51 [e.g. *Guéguen et al., 1986; Darot and Reuschlé, 2000; Guéguen et al., 2011; Nicolas et al.,*
52 *2014*]. The sustainability of fracture permeability under varying pressure is questionable
53 [e.g. *Zimmermann et al., 2010; Kluge et al., 2017*]. When compaction is taking place,
54 permeability can decrease with increasing deformation and damage [e.g. *Fortin et al.,*
55 *2005; Farquharson et al., 2017*].

56 Permeability evolution as a function of stress and strain in volcanic rocks has already been
57 studied and can decrease [e.g. *Farquharson et al., 2017*] or increase [e.g. *Farquharson et al.,*
58 *2016b*] with increasing axial strain. Moreover, in active volcanic hydrothermal systems,
59 rocks can have very different petrophysical properties. For example, *Heap et al. [2017]*
60 showed that the porosity of the materials in an active volcanic hydrothermal system (in
61 this study the Whakaari stratovolcano) varies from 0.01 to 0.7 and permeability varies by
62 eight orders of magnitude (from 10^{-19}m^2 to 10^{-11}m^2). The authors assumed that the wide
63 range in physical and hydraulic properties is the result of the numerous lithologies and
64 their varied micro-structures and alteration intensities. Finally, some post-earthquake
65 ground movement might be correlated to pore-pressure transients [e.g. *Jonsson et al.,*
66 *2003*], implying that pore pressure pulse diffusion under varying permeability conditions
67 is of interest.

68 Fibre optic pressure sensors are used in boreholes to record pressure with a high sensitivity
69 [e.g. *Reinsch and Henniges, 2010; Reinsch et al., 2013a, 2017*]. Fibre optic Fabry-Perot
70 interferometer diaphragm and the method of measurement is known since the early 20th

71 century, but to the authors' knowledge, were not widely used in laboratory experiments
72 [e.g. *Reinsch et al.*, 2012a; *Blöcher et al.*, 2014].

73 In the frame of the GEOTREF project, aiming at improving our understanding of the
74 behaviour of fractured geothermal reservoirs, this study focuses on the hydro-mechanical
75 behaviour of a low porosity andesite rock. Samples were heat-treated to 930°C to induce
76 thermal cracks and increase their permeability. The questions we address are: How does
77 a pulse of pore pressure propagate in a low porosity and low permeability rock? What are
78 the induced spatial distribution and evolution of the permeability under hydrostatic and
79 triaxial conditions? Can fibre optic Fabry-Perot interferometer diaphragms be used in
80 laboratory rock deformation experiments to record local pore pressure evolution and non-
81 linear diffusion of pore pressure? We report results of local pore pressure and permeability
82 measurements during a pore pressure pulse propagation under hydrostatic ($P_c=40$ MPa)
83 and triaxial stress states ($P_c=40$ MPa, differential stress of 356 MPa).

2. Sample characterization and experimental apparatus

2.1. Rock material and sample preparation

84 A cylindrical sample (length=100mm, diameter=50mm) was cored from a block of
85 andesite recovered from an outcrop in Anse a la Barque (Guadeloupe, French West Indies)
86 and the end-faces were ground flat to ensure a good parallelism. This andesite is formed
87 of a groundmass (composed of small crystals) with large phenocrysts (from hundreds of
88 microns to a few millimetres for the largest plagioclases) commonly micro-cracked (Figure
89 1 A and B). No obvious bedding related to volcanic features is identified in the block. The
90 sample has a connected porosity of less than 1% as measured using a pulse method. Initial
91 P-wave velocity in the sample was measured at room pressure and temperature and was
92 around 5000 m/s. Permeability is in the order of 10^{-21}m^2 as measured using a constant
93 flow procedure [*Li et al.*, 2019]. To induce thermal cracks and increase its permeability

94 before the experiment, the sample was heat-treated with a programmable Meker MHT-3
95 furnace [Nicolas *et al.*, 2014]. The sample was heated at a rate of 50 °C/h, up to 930
96 °C, kept 2 h at this temperature, and then cooled at 50 °C/h, to avoid any quenching
97 or thermal shock effect. Details on this procedure applied on andesite and associated
98 discussion can be found in Li *et al.* [2019]. The sample shows a higher fracture density
99 after heat treatment at 930 °C compared with intact samples (Figure 1). Heat treatment
100 induces a decrease of P-wave velocities to approximately 2900 m/s and an increase of
101 permeability to 10^{-15} m² measured using a constant flow procedure [Li *et al.*, 2019], as
102 also observed by Darot *et al.* [1992] among others. The intense micro-fracturing is due
103 to the different thermal expansion coefficients of the minerals [Fredrich and Wong, 1986;
104 Browning *et al.*, 2016].

2.2. Experimental apparatus and fibre optic sensor recording system

105 The sample was deformed in a conventional triaxial testing device (MTS 815) installed
106 at the GFZ Postdam (Germany). Details on the triaxial apparatus can be found in
107 Blöcher *et al.* [2007]. A shrinking tube made of fluorinated ethylene propylene (FEP)
108 was used during measurements of permeability evolution under hydrostatic loading and
109 neoprene jackets were used during pore pressure pulse propagation experiments to sepa-
110 rate the sample from the oil confining medium. Axial and radial strains were recorded
111 with two axial extensometers and one radial chain extensometer directly attached to the
112 jacket. Axial displacement was also measured with displacement transducers (DCDT)
113 mounted between the moving piston and a fixed platen. Volumetric strain is calculated
114 as $\varepsilon_v = \varepsilon_{ax} + 2\varepsilon_r$ where ε_{ax} and ε_r are the axial and radial strains, respectively. From now
115 on, compressive stresses and compactive strains are defined as positive.

116 Besides the mechanical system, an independent hydraulic system dedicated to pore pres-
117 sure was connected to the sample. Pore pressure and fluid flow can be controlled at the top

118 and the bottom of the sample with two servo-controlled micro-volumetric pumps (Quizix
119 6000-Series) coupled by pairs with an accuracy of about 10^{-2} MPa and 10^{-4} ml/min,
120 respectively [e.g. *Blöcher et al.*, 2014]. The total capillary void space between the pumps
121 and the sample is approximately 100 ml. The triaxial cell is equipped with a heating
122 system. The temperature inside the vessel is recorded by two thermo-couples plunged in
123 the confining oil close to the sample [e.g. *Pei et al.*, 2017].

124 The fibre optic sensors used in this study consist of miniature all-silica extrinsic Fabry-
125 Perot cavity interferometer (EFPI) pressure sensors. Monochromatic light is sent in the
126 fibre and propagates to its head. Incident light is reflected two times: (1) it is first partly
127 reflected at the entrance into the EFPI cavity (glass/air interface) and (2) the transmit-
128 ted light becomes reflected at the termination of the cavity (air/glass interface). Light
129 reflected from the end of the cavity is partly transmitted back into the fibre and interferes
130 with light reflected from the first reflection at the entrance into the Fabry-Perot cavity.
131 The phase shift between the two reflected signals depends on the cavity length, which is
132 a function of pressure and temperature, the latter being maintained constant at 30 °C
133 during all the experiments. Before being used, the fibre optic sensors have to be calibrated
134 (see next section), that is to say that the relation between pressure and cavity length (and
135 thus the phase shift evolution with pressure) has to be known through a calibration. A
136 thorough theoretical discussion of the principle of this sensor can be found in *Bremer*
137 *et al.* [2010] and details on the experimental set-up are given in *Reinsch et al.* [2012a, b].
138 Feedthroughs constructed in-home were specifically dedicated to let fibre optics enter the
139 pressure vessel [*Reinsch et al.*, 2013b]. To measure the pore pressure in the rock specimen
140 submitted to confining pressure, three fibre optic sensors were placed into three holes that
141 were previously drilled through the neoprene jacket in the rock at 1/4, 2/4 and 3/4 of
142 the height of the sample (Figure 2). The combination of the fibre optic sensors with the

143 pressure sensors of the Quizix system allow five independent pressure measurements at
144 five points along the sample (0, 25, 50, 75 and 100 mm).

2.3. Calibration of the fibre optic sensors

145 Before using the fibre optic sensors, these sensors had to be calibrated. For calibration,
146 the three fibre optic sensors were placed within the oil in the pressure chamber. Tem-
147 perature of the oil was controlled and maintained constant at 30 °C. The pressure was
148 increased from 2 to 40 MPa at a rate of 0.25 MPa/min in the vessel while data from the
149 sensors was recorded with a temporal resolution of 15 s, that is to say one measurement
150 approximately each 0.06 MPa. The sensor responses to an increase of pressure were tested
151 and the sensors response is shown to be linear as a function of pressure (Figure 3) for two
152 of the sensors (Fibres 1 and 3). Fibre 2 shows a hysteresis that could be explained by
153 a small leak in the Fabry-Perot cavity. The response of Fibre 2 seems to be correct and
154 linear after an initial non-linear response (Figure 3). From now on, this sensor will be
155 used only in the linear response domain and all pressure calculations are derived by the
156 slope of the calibration.

157 With the calibration information, it is possible to correlate phase shift changes to pres-
158 sure changes. Calibration information was then used to infer the pressure evolution as a
159 function of the sensor responses during the experiments. Based on the hysteresis of fibres
160 1 and 3, the precision can be estimated to be around 0.5 MPa. It is more complicated to
161 estimate the precision of fibre 2, and the response of this fibre will always be shown as a
162 dashed line.

3. Experimental procedures

163 In this section, we outline the experimental procedures used to monitor (1) the evolution
164 of porosity and permeability during hydrostatic loading (section 3.1), (2) the pore pressure

165 evolution while a pore pressure pulse is sent under hydrostatic pressure (section 3.2), and
 166 (3) the pore pressure evolution while a pore pressure pulse is sent under triaxial stresses
 167 (section 3.3). One single sample was used for the three different phases of the experiment.
 168 Temperature of the oil was controlled and maintained constant at 30 °C during all the
 169 phases of the experiments.

3.1. Measuring the evolution of porosity and permeability during hydrostatic loading

170 3.1.1. Experimental procedure for hydrostatic loading

The dry sample was first placed in the chamber and vacuumed to approximately 10 mbar. It was then loaded hydrostatically up to a pressure of 2 MPa and saturated with deionized water. Saturation was controlled with the micro-volumetric pumps. Full saturation was assumed to be reached when the total injected volume of water remained constant. The sample was loaded hydrostatically up to a confining pressure of 40 MPa at a controlled pressure increase rate of approximately 0.25 MPa/min, which leads to a maximum volumetric strain rate of approximately $4.4 \times 10^{-7} \text{s}^{-1}$ if we consider a bulk modulus of $K = 9.5 \text{ GPa}$ (as measured, see section 4.1). The characteristic time t to reach fluid pressure equilibrium for a diffusion process over a distance l can be approximated by [Carslaw and Jaeger, 1959; Ge and Stover, 2000; Duda and Renner, 2013; Nicolas et al., 2016]:

$$t \sim \frac{l^2}{D}, \quad (1)$$

where D is the hydraulic diffusivity. The hydraulic diffusivity D can be calculated as [Kümpel, 1991]:

$$D \sim \frac{kBK_d}{\eta\alpha}, \quad (2)$$

171 where k is the permeability, B is Skempton's coefficient, K_d is the drained bulk modulus,
 172 η is the fluid viscosity, and α is Biot's coefficient. For heat-treated andesite saturated

173 with water, $k = 10^{-17} \text{ m}^2$ (lowest value of permeability measured during hydrostatic
 174 loading, see section 4.1), $\eta = 1.002 \times 10^{-3} \text{ Pa}\cdot\text{s}$, and $K_d = 9.5 \text{ GPa}$. Assuming that
 175 Skempton's coefficient and Biot's coefficient are of the order of unity, hydraulic diffusivity
 176 is $D \sim 9.5 \cdot 10^{-7} \text{ m}^2\text{s}^{-1}$. The length of the sample is $l = 10 \text{ cm}$, and thus the diffusion
 177 time is in the order of $t \sim 100 \text{ s}$, which is a shorter time than hydrostatic loading time
 178 ($t \sim 10000 \text{ s}$) and ensures a fully drained behaviour.

179 Once the confining pressure of 40 MPa was reached, the sample was hydrostatically un-
 180 loaded using the same procedure as that used for loading. The sample is then removed
 181 from the pressure vessel and three holes are drilled to place the three fibre optic sensors
 182 (see section 2.2).

183 3.1.2. Permeability measurements during hydrostatic loading

During hydrostatic loading, permeability is continuously recorded. To do so, the hy-
 draulic short-cut (capillary connection) between the two ends of the sample were hy-
 draulically disconnected. Pore pressure was kept at a constant pressure of 0.2 MPa on
 the downstream side and a constant flow was applied on the upstream side of the sample.
 First a constant flow of 0.4 ml/min was used, and was then decreased to 0.05 ml/min,
 0.025 ml/min and finally 0.01 ml/min, as permeability decreased and to prevent upstream
 pressure to overcome confining pressure. A constant flow of 0.01 ml/min was used during
 complete unloading. Pore pressure increased on the side at which the flow was applied
 and permeability was calculated using Darcy's law [*Darcy*, 1856]:

$$k = \frac{Q\eta L}{A\Delta P}, \quad (3)$$

184 where k is the permeability, Q is the flow through the sample, η is the fluid viscosity, L is
 185 the length of the sample, A is the sample cross-sectional area and ΔP is the pore pressure
 186 differential.

187 3.1.3. Can compaction induce a flow comparable to the imposed one?

Using the experimental procedure described above, a remaining question is whether compaction could lead to a flow comparable to the one imposed by the permeability measurement [e.g. *Faulkner and Rutter*, 2003; *Mitchell and Faulkner*, 2008; *Crawford et al.*, 2008; *Fortin et al.*, 2011]. Volumetric strain rate is calculated as a function of imposed hydrostatic stress rate and bulk modulus as follows:

$$\dot{\epsilon}_v = \frac{\dot{P}}{K}, \quad (4)$$

where \dot{P} is the controlled pressure increase rate. Compactive volume rate is then simply calculated as:

$$\Delta\dot{V} = V\dot{\epsilon}_v, \quad (5)$$

188 where V is the volume of the sample. Using $V = 200\text{ml}$ and $\dot{\epsilon}_v = 2.6 \times 10^{-5}\text{min}^{-1}$, it
 189 yields an approximate compactive volume rate of $\Delta\dot{V} = 5 \times 10^{-3} \text{ ml/min}$. This approxi-
 190 mate (upper bound) compactive volume rate is twice lower than the imposed flow for the
 191 permeability measurement in the sample. Assuming a Biot's coefficient close to unity will
 192 forward the bulk volume rate to the fluid volume rate. For higher loads, Biot's coefficient
 193 will decrease, leading to a reduction of the fluid volume rate induced by compaction.
 194 To confirm that the compactive volume rate is lower than the imposed flow for the per-
 195 meability measurement, following *Fortin et al.* [2011], we consider that the fluid flow due
 196 to the compaction of the sample occurs on both sides of the sample. The rate of fluid
 197 volume output due to porosity compaction can simply be calculated as the mean of the
 198 fluid flow on both sides of the sample. Upstream imposed flow and downstream flow
 199 are significantly higher than compactive volume rate (mean flow) as shown in Figure 4,
 200 implying that permeability can be calculated with the imposed flux and neglecting the
 201 output of fluid due to porosity volume changes.

3.2. Pore pressure pulse under hydrostatic conditions

202 The pore pressure pulse propagation experiment was performed at a confining pressure
203 of 40 MPa. Once the fibre optic sensors were plugged in the previously 25 mm deep drilled
204 holes, the dry sample was first placed in the pressure vessel and loaded isostatically up to
205 a pressure of 2 MPa. Vacuum was then applied in the total pore pressure system. Once
206 a pore pressure of 0.01 bar was attained, the sample was saturated with deionized water.
207 Pore pressure was then maintained constant at 0.2 MPa on both sides of the sample.
208 Saturation was controlled with the micro-volumetric pumps. Full saturation was assumed
209 to be reached when the total injected volume of water remained constant.

210 Once full saturation was reached, pore pressure was maintained constant at a pressure of
211 0.2 MPa on both sides of the sample and the hydrostatic pressure was increased from 2
212 MPa to 40 MPa at a controlled pressure increase rate of approximately 0.25 MPa/min,
213 ensuring a fully drained behaviour (see section 3.1.1). When the total injected volume of
214 pore water remained constant, the hydraulic short-cut (capillary by-pass) between the two
215 ends of the sample were hydraulically disconnected and pore pressure was increased from
216 0.2 MPa to 20 MPa (in a few seconds) and kept constant at 20 MPa on the bottom side
217 of the sample (from now on called upstream) while the other pump (from now on called
218 downstream) was stopped and did not regulate the pore pressure. Downstream pump was
219 used to record the evolution of the pore pressure on this side of the sample. Pore pressure
220 evolution was recorded on both sides of the sample with the Quizix pumps and on three
221 points along the sample with the fibre optic sensors, leading to five independent pressure
222 measurements along the sample (0, 25, 50, 75 and 100 mm).

223 Once pore pressure reaches equilibrium in the whole sample, pore pressure was decreased
224 and maintained constant at a pressure of 0.2 MPa on the downstream side of the sample
225 while the pump situated on the upstream side was stopped. Finally, 35 minutes later,

226 pore pressure was decreased and maintained constant at a pressure of 0.2 MPa on both
227 sides of the sample.

3.3. Pore pressure pulse under triaxial stresses

228 First, the saturated sample was maintained under a hydrostatic pressure of 40 MPa
229 following the procedure described in section 3.2. Then, differential stress was applied by
230 axially loading the sample at a controlled stress rate of $\sim 10^{-1}\text{MPas}^{-1}$ until a differen-
231 tial stress of 356 MPa was attained. This controlled stress rate ensures a fully drained
232 behaviour during loading. Under the target differential stress, the sample remains in the
233 elastic domain as shown by the results released in *Li et al.* [2019]. Once the target dif-
234 ferential stress was reached, the stress-state was maintained constant. The two ends of
235 the sample were hydraulically disconnected and a pressure pulse was then induced. Pore
236 pressure was increased from 0.2 MPa to 35 MPa (in a few seconds) and kept constant at
237 35 MPa on the upstream side of the sample while the downstream pump was stopped.
238 Again, the pore pressure evolution was recorded on both sides of the sample with the
239 Quizix pumps and on three points along the sample with the fibre optic sensors, leading
240 to five independent pressure measurements along the sample (0, 25, 50, 75 and 100 mm).

4. Results

4.1. Hydrostatic loading: compaction and permeability evolution

241 Results for the hydrostatic loading and unloading experiment with up to 40 MPa con-
242 fining pressure are presented in Figure 5 (a). During loading, the hydrostatic response
243 was non-linear up to a pressure of ~ 28 MPa, beyond which the stress-strain curve be-
244 came almost linear with a slope corresponding to a static bulk modulus of approximately
245 $K = 9.5$ GPa (Figure 5 a). The mechanical response of heat-treated andesite subjected
246 to isostatic loading is typical of a rock with micro-cracks [*Walsh, 1965*]. The non-linearity

247 observed below 28 MPa can be explained by the progressive closure of pre-existing micro-
248 cracks [e.g. *Walsh, 1965; Batzle et al., 1980; Baud et al., 2000; Vajdova et al., 2004; Nicolas*
249 *et al., 2016*], such as the ones shown in Figure 1 (B, C and D). All cracks are considered
250 to be closed at an isostatic stress above 28 MPa. Comparing the volumetric strain mea-
251 sured and the perfectly elastic trend, micro-crack porosity can be estimated to be at least
252 $mp \sim 0.17\%$ [*Walsh, 1965*]. During unloading, the hydrostatic response was non-linear
253 and volumetric strain did not reach 0 when pressure reached 2 MPa.

254 As pressure was increased from 2 to 40 MPa, permeability decreased from $8 \times 10^{-16}\text{m}^2$
255 to $1.5 \times 10^{-17}\text{m}^2$ (Figure 5 b). Together with the static measurements, this decrease
256 highlights the closure of pre-existing cracks [e.g. *Brace et al., 1968; Brace, 1977, 1978*] be-
257 tween 0 and 40 MPa and more especially between 2 MPa and 28 MPa when the decrease
258 is more dramatic. During unloading, permeability increased from its minimum value to
259 $2 \times 10^{-16}\text{m}^2$ (Figure 5 b) but did not recover its initial value. This hysteresis, together
260 with the mechanical data, implies that some micro-cracks remain closed after the loading-
261 unloading procedure.

262 The evolution of permeability as a function of volumetric strain is strictly identical during
263 loading and unloading (Figure 5 c), showing that the cracks that remaining closed after
264 unloading are responsible for the permanent decrease of permeability after unloading.

4.2. Pore pressure propagation under hydrostatic stress

265 Local pore pressure measurements with fibre optic sensors as a function of time are
266 presented in Figure 6 (a). In addition, the evolution of upstream and downstream pore
267 pressures in the pumps are plotted in blue and black, respectively. During the whole
268 pressure pulse propagation, hydrostatic pressure was 40 MPa. Figure 6 (b) shows a linear
269 interpolation of pore pressure along the sample as a function of time. Magnifications of
270 the behaviour at the beginning of the experiment are provided in Figure 6 (c to f). When

271 pore pressure was increased upstream, the fibre optic sensors reacted one after the other
272 as a function of their location along the sample (Figure 6). They first showed a sudden
273 increase to intermediate values ranging from 15 MPa (the nearest from upstream) to
274 approximately 5 MPa (nearest to downstream). Downstream pore pressure increase was
275 very smooth (Figure 6 a). Fibre optic pressure measurements remained between the two
276 extremes (downstream and upstream) pore pressures, indicating a pressure gradient along
277 the sample. After 28 minutes, pore pressure was almost constant in the whole sample at
278 values around 19 to 20 MPa.

279 Then, pore pressure was decreased suddenly at the former downstream point (Figure 6
280 (a)), leading to a negative pore pressure pulse symmetrical to the positive pulse sent at
281 the beginning of the experiment. Pore pressure decreased and similar to the first part
282 of the experiment, a pore pressure gradient was highlighted. After 35 minutes, one can
283 observe a small positive pore pressure pulse during global pore pressure decrease, which
284 is due to the opening of a valve outside the sample.

285 After 65 minutes, pore pressure was maintained at 0.2 MPa on both sides of the sample.
286 The fibre optic sensors showed a progressive decrease of pore pressure in the sample. The
287 middle fibre optic sensor did not decrease to zero, which could be due to its hysteresis
288 shown during the calibration (section 2.3).

4.3. Pore pressure propagation under triaxial stresses

289 Figure 7 (a) shows the evolution of differential stress and volumetric strain during tri-
290 axial loading at a confining pressure of 40 MPa. During differential stress loading from 0
291 MPa to 356 MPa, volumetric strain is very low, in agreement with the hydrostatic me-
292 chanical results showing that pre-existing cracks were closed.

293 Before pore pressure pulse propagation, it was necessary to check that the sample was
294 not creeping (see *Brantut et al. [2013]* or *Nicolas et al. [2017]* for details on creep) under

295 a confining pressure of 40 MPa and a differential stress of 356 MPa. Figure 7 (b) shows
296 that axial and volumetric strains were extremely low (tending to 0) implying that there
297 was no creep.

298 When pore pressure was increased upstream, the fibre optic sensors reacted one after the
299 other as a function of their location along the sample but downstream pressure remained
300 at 0 MPa (Figure 8). The fibre optic sensors first showed a sudden increase to intermediate
301 values ranging from 7.5 MPa (the nearest from downstream) to approximately 27.5 MPa
302 (nearest to upstream). Pore pressure increase downstream was almost zero because pore
303 pressure at the upstream side was decreased before it started increasing downstream (Fig-
304 ure 8). Pore pressures then remained constant during more than 50 minutes and between
305 the two extreme (downstream and upstream) pore pressures. The gradient of pressure was
306 approximately constant within the sample although effective pressure increased from the
307 upstream side to the downstream side. After 55 minutes, pore pressure was maintained
308 at 0.2 MPa at the former upstream point and pore pressure started to decrease all over
309 the sample (Figure 8). The behaviour was similar as that observed under hydrostatic
310 pressure, with the sudden decrease followed by a gradual decrease.

5. Discussion

5.1. Permeability evolution under hydrostatic stress

The mechanical response of the heat-treated andesite subjected to isostatic loading (Figure 5 a) is typical for a rock with micro-cracks and pores [e.g. *Walsh*, 1965], in agreement with micro-structural observations of the intact heat-treated rock (Figure 1). The non-linearity in the stress-strain relation indicates crack closure up to a hydrostatic stress of 28 MPa, leading to a decrease of permeability from $8 \times 10^{-16} \text{m}^2$ to $1.5 \times 10^{-17} \text{m}^2$ which is similar to previous observations [e.g. *Vinciguerra et al.*, 2005; *Guéguen et al.*, 2011; *Nara et al.*, 2011].

At crack closure, permeability was about $1.5 \times 10^{-17} \text{m}^2$, whereas the thermally untreated sample had a permeability of approximately 10^{-21}m^2 . At crack closure, the difference to the thermally untreated sample remained around four orders of magnitude, as also observed by *Nara et al.* [2011]. This could be explained by the fact that cracks may be "mechanically closed", that is to say that asperities on both sides of the crack are in contact but there remains some open space between the asperities as observed by *Kranz et al.* [1979]; *Bernabe* [1986] and modelled by *Walsh* [1981]; *Zimmerman et al.* [1992]. *Sevostianov and Kachanov* [2002] showed that asperities in contact (also called islands) dominate the mechanical response.

To interpret theoretically and quantitatively the decrease of volumetric strain and permeability, we consider a porous rock as made of a mixture of solid matrix, spherical pores and penny-shaped cracks. Following *Walsh* [1965], the crack closure pressure P_{cl} for an isotropic stress state can be related to the crack aspect ratio defined as $\xi = w/2c$, where w and $2c$ are the crack aperture and the crack length, respectively :

$$\xi = \frac{4P_{cl}(1 - \nu_0^2)}{\pi E_0}, \quad (6)$$

where E_0 and ν_0 are the bulk moduli and Poisson's ratio of the crack-free matrix, respectively. Using the elastic properties of the crack-free material ($E_0 = 50 \text{ GPa}$ and $\nu_0 = 0.25$, which are standard values) and a crack closure pressure of $P_{cl} = 28 \text{ MPa}$, equation 6 gives an aspect ratio equal to $\xi = 7 \times 10^{-4}$, in good agreement with values reported in the literature [e.g. *Fontaine et al.*, 2008; *Adelinet et al.*, 2010; *Guéguen et al.*, 2011]. *Adelinet et al.* [2011] showed that at larger scale, aspect ratios are higher, highlighting that the aspect ratios could be scale-dependent in volcanic rocks. If cracks are assumed to be characterized by a penny-shape geometry, then crack porosity is given by [*Guéguen and Kachanov*, 2011]:

$$\phi^{crack} = 2\pi\rho_c\langle\xi\rangle, \quad (7)$$

where $\langle \xi \rangle$ is the average crack aspect ratio defined as $\langle \xi \rangle = \langle w/2c \rangle$ and ρ_c is the crack density defined as:

$$\rho_c = \frac{1}{V} \sum_{i=1}^n c_i^3, \quad (8)$$

where c_i is the radius of the i th crack and N is the total number of cracks embedded in the representative elementary volume (REV) V . Taking $\langle \xi \rangle = 7 \times 10^{-4}$ and an initial crack porosity $mp \simeq 0.17\%$ (determined from hydrostatic loading mechanical data shown in Figure 5 a), one finds an initial crack density equal to $\rho_c = 0.39$.

Dienes et al. [1982] calculated the permeability of a medium containing an isotropic distribution of cracks of radius c and found that:

$$k = \frac{32\pi}{15} \xi^3 c^2 \rho_c \theta f, \quad (9)$$

311 where θ and f are accounting for the hydrodynamics of flow through a system of cracks
 312 with varying thickness and accounting for the fraction of cracks that belong to an infinite
 313 network and will be determined from percolation theory, respectively. The percolation
 314 threshold calculated by *Guéguen and Dienes* [1989] for the case of a Bethe lattice where
 315 each crack has 4 neighbours is a crack density of approximately 0.14, much lower than
 316 the crack density of 0.39 calculated for our heat-treated andesite. Above the percolation
 317 threshold, the function f is equal to 1, which is the value used here. The factor θ ac-
 318 counting for the hydrodynamics of flow through a system of cracks with varying thickness
 319 is taken equal to 1 here, in agreement with *Guéguen and Dienes* [1989]. Using equation 9
 320 with $k = 10^{-17} \text{m}^2$, $\langle \xi \rangle = 7 \times 10^{-4}$ and $\rho_c = 0.39$, the mean crack length c can be calculated
 321 to be around 0.1 mm, which is in good agreement with direct observations (Figure 1 C
 322 and D) and corresponding to the average crystal length.

5.2. Describing fluid pressure pulse propagation under hydrostatic stress

It is now well-accepted that effective pressure has an influence on permeability [e.g. *Brace et al.*, 1968; *Brace*, 1977, 1978] and that the effective stress law for the permeability is not straightforward [e.g. *Ghabezloo et al.*, 2009; *Braun et al.*, 2018]. This is due to the potential closure of pre-existing cracks [e.g. *Brace et al.*, 1968; *Brace*, 1977, 1978]. Thus, pressure pulse propagation could lead to variations of permeability due to effective pressure variations.

Combining mass conservation and Darcy's law (equation 3) and neglecting fluid and rock compressibilities, fluid propagation can be modelled with a simple 1D diffusion equation [e.g. *Rice and Cleary*, 1976]:

$$\frac{\partial p(z)}{\partial z} = C(t), \quad (10)$$

where C is a constant. Neglecting rock compressibility may be a strong assumption, but this can be verified using the fibre optic sensors and comparing their measurements to the pore pressure evolution at specific positions (corresponding to those of the fibre optic sensors) calculated with a constant pore pressure gradient derived from pressure values in the upstream and downstream pumps (Figure 9 a). A zoom into the beginning of the pressure pulse is provided in Figure 9 (b). Calculated pore pressures are close to measured data, showing that the pore pressure evolution follows an evolving constant gradient along the sample during pore pressure increase and decrease, in agreement with equation 10. Assuming a constant flow along the sample (*i.e.*, steady state or neglected fluid compressibility), local pore pressure measurements and Darcy's law were used to calculate the evolution of permeability along the sample as a function of time (Figure 9 c). Local permeability measurements are in good agreement with the mean permeability calculated from upstream and downstream pump pressure measurements (light blue in Figure 9 c). Fibre 2 may not be very reliable (section 2.3) and permeabilities calculated with this fibre could not be considered. Permeability calculated between upstream and fibre 1 is lower

338 than permeability calculated between fibre 3 and downstream, implying that permeability
339 could decrease with decreasing effective pressure. Permeability calculated between fibres
340 1 and 3 (purple points in Figure 9 c) is comprised between the previous permeabilities.
341 Comparison between these three permeabilities may not be reliable because the fibre optic
342 sensor measurements have a precision that can be estimated to be around 0.5 MPa (see
343 section 2.3). The evolution of permeability as a function of time for one section of the
344 sample is possible to consider. Permeability calculated in the section of the sample nearest
345 to the downstream side increases with pore pressure, due to crack opening with effective
346 pressure decrease due to pore pressure increase (black dots in Figure 9 c). Permeability
347 calculated in the section of the sample nearest to the upstream side remained constant
348 as a function of time (blue dots in Figure 9 c), which can be explained by the fact that
349 pore pressure remained almost constant in this part of the sample. The mean permeabil-
350 ity calculated between the upstream and downstream pumps is always between the local
351 permeability measurements. Finally, when pore pressure was almost at equilibrium, local
352 pore pressure measurements were not precise enough to calculate local permeabilities.
353 However, this pore pressure pulse propagation experiment highlights the interest of the
354 use of fibre optics to measure local pore pressures.

5.3. Modelling pore pressure increase in a disconnected dead volume

Following *Mayr et al.* [2011], the experiments were modelled considering the diffusion of water from the upstream side, through the sample and into the downstream dead volume (tubing and pump) as shown in Figure 10. Neglecting fluid compressibility but removing the hypothesis that rock compressibility can be neglected compared to equation 10, fluid propagation can be modelled with a new diffusion equation. During pore fluid migration, pore pressure p in the sample depends on the distance from upstream z and time t , which

can be described by a 1D version of the diffusion equation [e.g. *Rice and Cleary, 1976*]:

$$\frac{\partial p(z, t)}{\partial t} = D \frac{\partial^2 p(z, t)}{\partial z^2}, \quad (11)$$

where D is the diffusivity.

Experimental results show that downstream dead volume controls the increase of pore pressure downstream and permeability is relatively high, implying that the gradient in the sample is controlled by the downstream dead volume. Let us examine the upstream and downstream boundary conditions. Initial pore pressure is equal to 0.2 MPa upstream, in the complete sample and in the downstream reservoir:

$$\forall z, p(z = 0, t < t_i) = 0.2 \text{MPa}, \quad (12)$$

where t_i is the time at which the pore pressure step is applied. Then, even though the upstream pressure application may be slightly delayed, the application of the pore pressure step upstream is simply approximated by a step function, such as:

$$p(z = 0, t \geq t_i) = 20 \text{MPa}. \quad (13)$$

Let us now examine the role of the downstream dead volume, as done by *Pimienta et al. [2016]*. We consider fluid mass continuity downstream, *i.e.*, the change of mass in the sample equals the fluid mass change in the dead volume, with opposite sign. Following *Brace et al. [1968]* and *Lin [1977]*, the downstream boundary condition is:

$$S_1 \frac{\partial p_d}{\partial t}_{z=L} + \frac{kA}{\eta} \frac{\partial p_p}{\partial z}_{z=L} = 0, \quad (14)$$

where L is the sample length, and S_1 is the downstream reservoir storage capacity. The storage capacity is:

$$S_1 = \frac{V_1}{K_f}, \quad (15)$$

where V_1 is the reservoir volume and K_f is the fluid bulk modulus. Note that we neglect the reservoir compressibility. Equations 11 and 14 are resolved with the boundary conditions expressed in equations 12, 13, and 14. Note that this implies that permeability is

358 considered constant during the complete experiment, whatever the effective pressure. We
359 thus neglect the permeability sensitivity to effective pressure.

360 The values of the parameters used in the model are given in Table 1. Rock porosity, bulk
361 modulus and intrinsic permeability are taken equal to those measured on heat-treated
362 samples. Fluid characteristics (bulk modulus, density and dynamic viscosity) are taken
363 equal to those of water commonly obtained at 20°C. Downstream volume was experimen-
364 tally measured on the machine. To sum up, the values used for the model are taken equal
365 to those experimentally obtained on rock samples, on the machine and values for fluid
366 (water) are taken from the literature.

367 Figure 11 shows the comparison between our experimental results and the model pre-
368 dictions. Predicted downstream pore pressure evolution (black curve) is in very good
369 agreement with the experimental results. However, pore pressure evolution at the three
370 points along the sample corresponding to the location of the fibre optic sensors are in
371 moderate agreement since the present model is not able to predict the sudden increase
372 to the intermediate values followed by a smooth increase to their maximum value. This
373 could be explained by the fact that the applied pore pressure pulse could act as a stress
374 boundary at the bottom of the sample (since it does not diffuse instantaneously). This ad-
375 ditional external stress could lead to a compression of the downstream part of the sample.
376 Due to poro-elastic behaviour, this additional compaction could lead to a sudden pore
377 pressure increase without diffusion, which was not considered by the simulation. Another
378 explanation could be that permeability evolution as a function of effective pressure (and
379 thus pore pressure) has to be taken into account in the model.

5.4. Implications and perspectives

380 The use of fibre optics to measure local pore pressure was shown to be useful to un-
381 derstand the hydro-mechanical behaviour of low-permeability porous materials. In this

382 study, fibre optics were used to monitor the migration of a pore pressure pulse but it also
383 opens new horizons for this technique, which are discussed below.

384 Pore pressure diffusion could also control the transmission of stress and the diffusing pore
385 pressure front could play a dual role in the triggering of seismicity by decreasing the co-
386 efficient of friction and by decreasing the strength [e.g. *Talwani and Acree*, 1984]. Excess
387 pore pressure can also cause an embrittlement of porous fluid-saturated media, as shown
388 by *Farquharson et al.* [2016a] in the case of volcanic edifices. Comparing pore pressure
389 migration with fibre optics and acoustic emission migration with an acoustic system could
390 help improving our understanding of triggered seismicity.

391 Rapid fault slip during earthquakes can increase pore pressure because of thermal pres-
392 surization, which can decrease shear resistance of the fault material [e.g. *Rempel and*
393 *Rice*, 2006; *Sulem et al.*, 2007], or pore pressure decrease because of the opening of new
394 fractures. It would be possible to use fibre optics during failure of samples to have a
395 closer look at pore pressure evolution during shearing inducing dilatancy and failure of
396 low-permeability porous media subjected to triaxial stresses. Fibre optics would be use-
397 ful to study the evolution of local pore pressure during laboratory stick-slip experiments
398 [e.g. *Passelègue et al.*, 2013] under water saturated conditions, which is similar to what is
399 observed on natural faults [e.g. *Passelègue et al.*, 2014].

400 Natural faults could control the pathways of fluids and thus fluid diffusion in geothermal
401 fields [e.g. *Brehme et al.*, 2016b]. Fibre optics can be used to monitor the evolution of
402 permeability in low-permeability saw-cut samples to study the evolution of permeability
403 of natural faults as a function of confining pressure and differential stress.

6. Conclusions

404 It is well known that pore pressure has a major influence on the mechanical behaviour
405 of porous rocks, and thus is of interest for industrial purposes and for our understanding

406 of natural events such as earthquakes. A key parameter for fluid pressure build up is the
407 ability for the material to diffuse fluid, that is to say permeability. However, permeability
408 can be very variable. In the heat-treated andesitic rock used in this study, permeability
409 decreased from $8 \times 10^{-16} \text{m}^2$ to $1.5 \times 10^{-17} \text{m}^2$ with a confining pressure increase from 2
410 MPa to 40 MPa. Moreover, a differential stress of 356 MPa decreased permeability from
411 10^{-17}m^2 to 10^{-19}m^2 .

412 In low permeability samples, fluid diffusion can be very slow, implying that it is hard to
413 follow from the sides of the sample, especially when there are large dead volumes. To
414 overcome this difficulty, we used fibre optic pressure sensors to monitor pore pressure
415 evolution as a function of time along the sample during the propagation of pore pressure
416 pulse under hydrostatic ($P_c=40$ MPa) and triaxial stress ($P_c=40$ MPa, differential stress
417 of 356 MPa). Finally, the pore pressure diffusion process was modelled considering a
418 uniform spatial distribution of permeability in the andesite sample and the dead volume
419 attached at the down-stream side. This modelling leads to results in very good agreement
420 with experimental results.

421 **Acknowledgments.** This work was completed when AN was a visiting researcher at
422 the Helmholtz Centre Potsdam - GFZ German Research Centre for Geosciences. AN
423 thanks all the members of GFZ Section 6.2 for their hospitality during his visit. AN's
424 visit was supported by a Programme Hubert Curien (PHC) Procope grant (Number
425 32989NB) set up by the Deutscher Akademischer Austausch Dienst (DAAD) in Germany
426 and by the Ministère de l'Europe et des Affaires étrangères (MEAE) and the Ministère
427 de l'Enseignement supérieur, de la Recherche et de l'Innovation (MESRI) in France.

428 This study was performed in the frame of the GEOTREF project, aiming at improving
429 our understanding of the behaviour of fractured geothermal reservoirs. The GEOTREF
430 project is a program supported by the ADEME, French environmental agency and by the

431 Investissement d’Avenir , a French government program to fund innovative projects.
432 AN is grateful to Harsha S. Bhat, Francois Passelègue and Alexandre Schubnel for stim-
433 ulating discussions. The authors are grateful to Damien Deldicque and Tanja Ballerstedt
434 for technical support, and to Christian Cunow who skillfully prepared the EFPI fibre optic
435 sensors.

436 The authors would like to acknowledge the constructive reviews provided by Dr Carolina
437 Giorgetti and one anonymous reviewer.

References

- 438 Adelinet, M., J. Fortin, Y. Guéguen, A. Schubnel, and L. Geoffroy (2010), Frequency and
439 fluid effects on elastic properties of basalt: Experimental investigations, *Geophysical*
440 *Research Letters*, *37*(2).
- 441 Adelinet, M., C. Dorbath, M. Le Ravalec, J. Fortin, and Y. Guéguen (2011), Deriving mi-
442 crostructure and fluid state within the Icelandic crust from the inversion of tomography
443 data, *Geophysical research letters*, *38*(3).
- 444 Batzle, M. L., G. Simmons, and R. W. Siegfried (1980), Microcrack closure in rocks under
445 stress: Direct observation, *Journal of Geophysical Research: Solid Earth*, *85*(B12),
446 7072–7090.
- 447 Baud, P., A. Schubnel, and T.-f. Wong (2000), Dilatancy, compaction, and failure mode
448 in Solnhofen limestone, *Journal of Geophysical Research: Solid Earth*, *105*(B8), 19,289–
449 19,303, doi:10.1029/2000JB900133.
- 450 Bemer, E., and J. Lombard (2010), From injectivity to integrity studies of CO₂ geologi-
451 cal storage chemical alteration effects on carbonates petrophysical and geomechanical
452 properties., *Oil Gas Sci. Technol.- Rev. IFP*, *65*, 445–459.

- 453 Bernabe, Y. (1986), The effective pressure law for permeability in Chelmsford granite
454 and Barre granite, in *International Journal of Rock Mechanics and Mining Sciences &*
455 *Geomechanics Abstracts*, vol. 23, pp. 267–275.
- 456 Blöcher, G., D. Bruhn, G. Zimmermann, C. McDermott, and E. Huenges (2007), In-
457 vestigation of the undrained poroelastic response of sandstones to confining pressure
458 via laboratory experiment, numerical simulation and analytical calculation, *Geological*
459 *Society, London, Special Publications*, 284(1), 71–87.
- 460 Blöcher, G., T. Reinsch, A. Hassanzadegan, H. Milsch, and G. Zimmermann (2014), Di-
461 rect and indirect laboratory measurements of poroelastic properties of two consolidated
462 sandstones, *International Journal of Rock Mechanics and Mining Sciences*, 67, 191–201.
- 463 Brace, W. (1977), Permeability from resistivity and pore shape, *Journal of Geophysical*
464 *Research*, 82(23), 3343–3349.
- 465 Brace, W. (1978), A note on permeability changes in geologic material due to stress, *Pure*
466 *and applied geophysics*, 116(4), 627–633.
- 467 Brace, W., J. Walsh, and W. Frangos (1968), Permeability of granite under high pressure,
468 *Journal of Geophysical research*, 73(6), 2225–2236.
- 469 Brantut, N., M. Heap, P. Meredith, and P. Baud (2013), Time-dependent cracking and
470 brittle creep in crustal rocks: A review, *Journal of Structural Geology*, 52, 17–43.
- 471 Braun, P., S. Ghabezloo, P. Delage, J. Sulem, and N. Conil (2018), Theoretical analysis
472 of pore pressure diffusion in some basic rock mechanics experiments, *Rock Mechanics*
473 *and Rock Engineering*, pp. 1–18.
- 474 Brehme, M., F. Deon, C. Haase, B. Wiegand, Y. Kamah, M. Sauter, and S. Regenspurg
475 (2016a), Geochemical properties controlled by fault permeability in a geothermal reser-
476 voir (Lahendong, Indonesia), *Grundwasser*, 21, 29–41.

- 477 Brehme, M., G. Blöcher, M. Cacace, Y. Kamah, M. Sauter, and G. Zimmermann (2016b),
478 Permeability distribution in the Lahendong geothermal field: A blind fault captured by
479 thermal-hydraulic simulation, *Environmental Earth Sciences*, 75(14), 1–11.
- 480 Bremer, K., E. Lewis, G. Leen, B. Moss, S. Lochmann, I. Mueller, T. Reinsch, and
481 J. Schroetter (2010), Fibre optic pressure and temperature sensor for geothermal wells,
482 in *Sensors, 2010 IEEE*, pp. 538–541.
- 483 Browning, J., P. Meredith, and A. Gudmundsson (2016), Cooling-dominated cracking in
484 thermally stressed volcanic rocks, *Geophysical Research Letters*, 43(16), 8417–8425.
- 485 Carslaw, H. S., and J. C. Jaeger (1959), Conduction of heat in solids, *Oxford: Clarendon*
486 *Press, 1959, 2nd ed., 1*.
- 487 Chanard, K., A. Nicolas, T. Hatano, F. Petrelis, S. Latour, S. Vinciguerra, and A. Schub-
488 nel (2019), Sensitivity of acoustic emission triggering to small pore pressure cycling
489 perturbations during brittle creep, *Geophysical Research Letters*, 46(13), 7414–7423.
- 490 Crawford, B., D. Faulkner, and E. Rutter (2008), Strength, porosity, and permeability
491 development during hydrostatic and shear loading of synthetic quartz-clay fault gouge,
492 *Journal of Geophysical Research: Solid Earth*, 113(B3).
- 493 Darcy, H. (1856), *Les fontaines publiques de la ville de Dijon: exposition et application...*,
494 Victor Dalmont.
- 495 Darot, M., and T. Reuschlé (2000), Acoustic wave velocity and permeability evolution
496 during pressure cycles on a thermally cracked granite, *International Journal of Rock*
497 *Mechanics and Mining Sciences*, 37(7), 1019–1026.
- 498 Darot, M., Y. Guéguen, and M. Baratin (1992), Permeability of thermally cracked granite,
499 *Geophys. Res. Lett.*, 19, 869–872.
- 500 David, C., T.-F. Wong, W. Zhu, and J. Zhang (1994), Laboratory measurement of
501 compaction-induced permeability change in porous rocks: Implications for the genera-

- tion and maintenance of pore pressure excess in the crust, *Pure and Applied Geophysics*,
143(1), 425–456.
- Deichmann, N., and D. Giardini (2009), Earthquakes induced by the stimulation of an
enhanced geothermal system below Basel (Switzerland), *Seismological Research Letters*,
80(5), 784–798.
- Dienes, J. K., et al. (1982), Permeability, percolation and statistical crack mechanics,
in *The 23rd US Symposium on Rock Mechanics (USRMS)*, American Rock Mechanics
Association.
- Duda, M., and J. Renner (2013), The weakening effect of water on the brittle failure
strength of sandstone, *Geophysical Journal International*, 192(3), 1091–1108.
- Farquharson, J., M. J. Heap, P. Baud, T. Reuschlé, and N. R. Varley (2016a), Pore
pressure embrittlement in a volcanic edifice, *Bulletin of Volcanology*, 78(1), 6.
- Farquharson, J. I., M. J. Heap, and P. Baud (2016b), Strain-induced permeability increase
in volcanic rock, *Geophysical Research Letters*, 43(22).
- Farquharson, J. I., P. Baud, and M. J. Heap (2017), Inelastic compaction and permeability
evolution in volcanic rock, *Solid Earth*, 8(2), 561–581.
- Faulkner, D., and E. Rutter (2003), The effect of temperature, the nature of the pore
fluid, and subyield differential stress on the permeability of phyllosilicate-rich fault
gouge, *Journal of Geophysical Research: Solid Earth*, 108(B5).
- Fontaine, F. R., D. R. Neuville, B. Ildefonse, and D. Mainprice (2008), Influence of melt
viscosity of basaltic and andesitic composition on seismic attenuation in partially molten
gabbro-norite, *Physics of the Earth and Planetary Interiors*, 167(3), 223–229.
- Fortin, J., A. Schubnel, and Y. Guéguen (2005), Elastic wave velocities and permeability
evolution during compaction of Bleurswiller sandstone, *International Journal of Rock
Mechanics and Mining Sciences*, 42(7), 873–889.

- 527 Fortin, J., S. Stanchits, S. Vinciguerra, and Y. Guéguen (2011), Influence of thermal and
528 mechanical cracks on permeability and elastic wave velocities in a basalt from Mt. Etna
529 volcano subjected to elevated pressure, *Tectonophysics*, *503*(1), 60–74.
- 530 Fredrich, J. T., and T.-f. Wong (1986), Micromechanics of thermally induced cracking
531 in three crustal rocks, *Journal of Geophysical Research: Solid Earth*, *91*(B12), 12,743–
532 12,764.
- 533 Ge, S., and S. C. Stover (2000), Hydrodynamic response to strike-and dip-slip faulting
534 in a half-space, *Journal of Geophysical Research: Solid Earth (1978–2012)*, *105*(B11),
535 25,513–25,524.
- 536 Ghabezloo, S., J. Sulem, S. Guédon, and F. Martineau (2009), Effective stress law for
537 the permeability of a limestone, *International Journal of Rock Mechanics and Mining*
538 *Sciences*, *46*(2), 297–306.
- 539 Guéguen, Y., and J. Dienes (1989), Transport properties of rocks from statistics and
540 percolation, *Mathematical geology*, *21*(1), 1–13.
- 541 Guéguen, Y., and M. Kachanov (2011), Effective elastic properties of cracked rocks - An
542 overview, *in*, *Mechanics of crustal rocks, CISM Courses and Lectures*, pp. 73–125.
- 543 Guéguen, Y., C. David, and M. Darot (1986), Models and time constants for permeability
544 evolution, *Geophysical Research Letters*, *13*(5), 460–463.
- 545 Guéguen, Y., M. Adelinet, A. Ougier-Simonin, J. Fortin, and A. Schubnel (2011), How
546 cracks modify permeability and introduce velocity dispersion: Examples of glass and
547 basalt, *The Leading Edge*, *30*(12), 1392–1398.
- 548 Häring, M. O., U. Schanz, F. Ladner, and B. C. Dyer (2008), Characterisation of the
549 Basel 1 enhanced geothermal system, *Geothermics*, *37*(5), 469–495.
- 550 Heap, M. J., B. M. Kennedy, J. I. Farquharson, J. Ashworth, K. Mayer, M. Letham-
551 Brake, T. Reuschlé, H. A. Gilg, B. Scheu, Y. Lavallée, et al. (2017), A multidisci-

- 552 plinary approach to quantify the permeability of the Whakaari/White Island volcanic
553 hydrothermal system (Taupo Volcanic Zone, New Zealand), *Journal of Volcanology and*
554 *Geothermal Research*, 332, 88–108.
- 555 Johann, L., C. Dinske, and S. Shapiro (2016), Scaling of seismicity induced by nonlinear
556 fluid-rock interaction after an injection stop, *Journal of Geophysical Research: Solid*
557 *Earth*, 121(11), 8154–8174.
- 558 Jonsson, S., P. Segall, R. Pedersen, and G. Björnsson (2003), Post-earthquake ground
559 movements correlated to pore-pressure transients, *Nature*, 424(6945), 179.
- 560 Katayama, I., A. Nicolas, and A. Schubnel (2018), Fluid-induced fracturing of initially
561 damaged granite triggered by pore pressure buildup, *Geophysical Research Letters*,
562 45(15), 7488–7495.
- 563 Kluge, C., G. Blöcher, H. Milsch, H. Hofmann, A. Nicolas, Z. Li, and J. Fortin (2017),
564 Sustainability of fractured rock permeability under varying pressure, in *Poromechanics*
565 *VI*, pp. 1192–1199.
- 566 Kranz, R., A. Frankel, T. Engelder, and C. Scholz (1979), The permeability of whole and
567 jointed Barre granite, in *International Journal of Rock Mechanics and Mining Sciences*
568 *& Geomechanics Abstracts*, vol. 16, pp. 225–234, Elsevier.
- 569 Kümpel, H.-J. (1991), Poroelasticity: parameters reviewed, *Geophysical Journal Interna-*
570 *tional*, 105(3), 783–799.
- 571 Li, Z., J. Fortin, A. Nicolas, D. Deldicque, and Y. Guéguen (2019), Physical and mechan-
572 ical properties of thermally cracked andesite under pressure, *Rock Mechanics and Rock*
573 *Engineering*, pp. 1–21.
- 574 Lin, W. (1977), Compressible fluid flow through rocks of variable permeability, *Tech. rep.*,
575 California Univ., Livermore (USA). Lawrence Livermore Lab.

- 576 Majer, E. L., R. Baria, M. Stark, S. Oates, J. Bommer, B. Smith, and H. Asanuma (2007),
577 Induced seismicity associated with enhanced geothermal systems, *Geothermics*, *36*(3),
578 185–222.
- 579 Mayr, S. I., S. Stanchits, C. Langenbruch, G. Dresen, and S. A. Shapiro (2011), Acoustic
580 emission induced by pore-pressure changes in sandstone samples, *Geophysics*, *76*(3),
581 21–32.
- 582 Miller, S. A. (2002), Properties of large ruptures and the dynamical influence of fluids
583 on earthquakes and faulting, *Journal of Geophysical Research: Solid Earth*, *107*(B9),
584 1–13, doi:10.1029/2000JB000032.
- 585 Mitchell, T., and D. Faulkner (2008), Experimental measurements of permeability evolu-
586 tion during triaxial compression of initially intact crystalline rocks and implications for
587 fluid flow in fault zones, *Journal of Geophysical Research: Solid Earth*, *113*(B11).
- 588 Nara, Y., P. G. Meredith, T. Yoneda, and K. Kaneko (2011), Influence of macro-fractures
589 and micro-fractures on permeability and elastic wave velocities in basalt at elevated
590 pressure, *Tectonophysics*, *503*(1-2), 52–59.
- 591 Nicolas, A., F. Girault, A. Schubnel, É. Pili, F. Passelègue, J. Fortin, and D. Deldicque
592 (2014), Radon emanation from brittle fracturing in granites under upper crustal condi-
593 tions, *Geophysical Research Letters*, *41*(15), 5436–5443.
- 594 Nicolas, A., J. Fortin, J. Regnet, A. Dimanov, and Y. Guéguen (2016), Brittle and semi-
595 brittle behaviours of a carbonate rock: influence of water and temperature, *Geophysical*
596 *Journal International*, *206*(1), 438–456.
- 597 Nicolas, A., J. Fortin, J. Regnet, B. Verberne, O. Plümper, A. Dimanov, C. Spiers, and
598 Y. Guéguen (2017), Brittle and semibrittle creep of tavel limestone deformed at room
599 temperature, *Journal of Geophysical Research: Solid Earth*, *122*(6), 4436–4459.

- 600 Passelègue, F. X., A. Schubnel, S. Nielsen, H. S. Bhat, and R. Madariaga (2013), From sub-
601 rayleigh to supershear ruptures during stick-slip experiments on crustal rocks, *Science*,
602 *340*(6137), 1208–1211.
- 603 Passelègue, F. X., O. Fabbri, M. Dubois, and S. Ventalon (2014), Fluid overpressure along
604 an Oligocene out-of-sequence thrust in the Shimanto Belt, SW Japan, *Journal of Asian*
605 *Earth Sciences*, *86*, 12–24.
- 606 Pei, L., G. Blöcher, H. Milsch, G. Zimmermann, I. Sass, and E. Huenges (2017), Thermo-
607 mechanical properties of Upper Jurassic (Malm) carbonate rock under drained condi-
608 tions, *Rock Mechanics and Rock Engineering*, pp. 1–23.
- 609 Pimienta, L., J. Borgomano, J. Fortin, and Y. Guéguen (2016), Modelling the
610 drained/undrained transition: effect of the measuring method and the boundary con-
611 ditions, *Geophysical Prospecting*, *64*(4), 1098–1111.
- 612 Reinsch, T., and J. Henniges (2010), Temperature-dependent characterization of optical
613 fibres for distributed temperature sensing in hot geothermal wells, *Measurement Science*
614 *and Technology*, *21*(9), 094,022.
- 615 Reinsch, T., G. Blöcher, H. Milsch, K. Bremer, E. Lewis, G. Leen, and S. Lochmann
616 (2012a), A fibre optic sensor for the in situ determination of rock physical properties,
617 *arXiv preprint arXiv:1208.1233*.
- 618 Reinsch, T., G. Blöcher, H. Milsch, K. Bremer, E. Lewis, G. Leen, and S. Lochmann
619 (2012b), A fibre optic sensor for the in situ determination of rock physical proper-
620 ties, *International Journal of Rock Mechanics and Mining Sciences*, *55*, 55 – 62, doi:
621 <https://doi.org/10.1016/j.ijrmms.2012.06.011>.
- 622 Reinsch, T., J. Henniges, and R. Ásmundsson (2013a), Thermal, mechanical and chem-
623 ical influences on the performance of optical fibres for distributed temperature sensing
624 in a hot geothermal well, *Environmental earth sciences*, *70*(8), 3465–3480.

- 625 Reinsch, T., C. Cunow, J. Schrötter, and R. Giese (2013b), Simple feed-through for cou-
626 pling optical fibres into high pressure and temperature systems, *Measurement Science*
627 *and Technology*, *24*(3), 037,001.
- 628 Reinsch, T., T. Thurley, and P. Jousset (2017), On the mechanical coupling of a fiber optic
629 cable used for distributed acoustic/vibration sensing applicationsa theoretical consider-
630 ation, *Measurement Science and Technology*, *28*(12), 127,003.
- 631 Rempel, A. W., and J. R. Rice (2006), Thermal pressurization and onset of melting in
632 fault zones, *Journal of Geophysical Research: Solid Earth*, *111*(B9).
- 633 Rice, J. R., and M. P. Cleary (1976), Some basic stress diffusion solutions for fluid-
634 saturated elastic porous media with compressible constituents, *Reviews of Geophysics*,
635 *14*(2), 227–241.
- 636 Segall, P., and S. D. Fitzgerald (1998), A note on induced stress changes in hydrocarbon
637 and geothermal reservoirs, *Tectonophysics*, *289*(1-3), 117–128.
- 638 Sevostianov, I., and M. Kachanov (2002), On elastic compliances of irregularly shaped
639 cracks, *International Journal of Fracture*, *114*(3), 245–257.
- 640 Shapiro, S., and C. Dinske (2009a), Scaling of seismicity induced by nonlinear fluid-rock
641 interaction, *Journal of Geophysical Research: Solid Earth*, *114*(B9).
- 642 Shapiro, S., and C. Dinske (2009b), Fluid-induced seismicity: Pressure diffusion and
643 hydraulic fracturing, *Geophysical Prospecting*, *57*(2), 301–310.
- 644 Shapiro, S., R. Patzig, E. Rothert, and J. Rindschwentner (2003), Triggering of seismicity
645 by pore-pressure perturbations: Permeability-related signatures of the phenomenon, in
646 *Thermo-Hydro-Mechanical Coupling in Fractured Rock*, pp. 1051–1066, Springer.
- 647 Shapiro, S. A., E. Huenges, and G. Borm (1997), Estimating the crust permeability from
648 fluid-injection-induced seismic emission at the KTB site, *Geophysical Journal Interna-*
649 *tional*, *131*(2).

- 650 Sulem, J., P. Lazar, and I. Vardoulakis (2007), Thermo-poro-mechanical properties of
651 clayey gouge and application to rapid fault shearing, *International journal for numerical
652 and analytical methods in geomechanics*, 31(3), 523–540.
- 653 Talwani, P., and S. Acree (1984), Pore pressure diffusion and the mechanism of reservoir-
654 induced seismicity, *Pure and Applied Geophysics*, 122(6), 947–965.
- 655 Terakawa, T., S. A. Miller, and N. Deichmann (2012), High fluid pressure and triggered
656 earthquakes in the enhanced geothermal system in Basel, Switzerland, *Journal of Geo-
657 physical Research: Solid Earth*, 117(B7).
- 658 Tester, J. W., B. J. Anderson, A. S. Batchelor, D. D. Blackwell, R. DiPippo, E. Drake,
659 J. Garnish, B. Livesay, M. C. Moore, K. Nichols, et al. (2006), The future of geothermal
660 energy: Impact of enhanced geothermal systems (EGS) on the United States in the 21st
661 century, *Massachusetts Institute of Technology*, 209.
- 662 Vajdova, V., P. Baud, and T.-F. Wong (2004), Compaction, dilatancy, and failure in
663 porous carbonate rocks, *Journal of Geophysical Research: Solid Earth*, 109(B5), doi:
664 10.1029/2003JB002508.
- 665 Vinciguerra, S., C. Trovato, P. Meredith, and P. Benson (2005), Relating seismic velocities,
666 thermal cracking and permeability in mt. etna and iceland basalts, *International Journal
667 of Rock Mechanics and Mining Sciences*, 42(7-8), 900–910.
- 668 Walsh, J. B. (1965), The effect of cracks on the compressibility of rock, *Journal of Geo-
669 physical Research*, 70(2), 381–389, doi:10.1029/JZ070i002p00381.
- 670 Walsh, J. B. (1981), Effect of pore pressure and confining pressure on fracture permeabil-
671 ity, in *International Journal of Rock Mechanics and Mining Sciences & Geomechanics
672 Abstracts*, vol. 18, pp. 429–435.
- 673 Zang, A., V. Oye, P. Jousset, N. Deichmann, R. Gritto, A. McGarr, E. Majer, and
674 D. Bruhn (2014), Analysis of induced seismicity in geothermal reservoirs—an overview,

- 675 *Geothermics*, 52, 6–21.
- 676 Zhu, W., and T.-f. Wong (1997), The transition from brittle faulting to cataclastic flow:
677 Permeability evolution, *Journal of Geophysical Research: Solid Earth*, 102(B2), 3027–
678 3041.
- 679 Zimmerman, R. W., D.-W. Chen, and N. G. Cook (1992), The effect of contact area on
680 the permeability of fractures, *Journal of Hydrology*, 139(1-4), 79–96.
- 681 Zimmermann, G., and A. Reinicke (2010), Hydraulic stimulation of a deep sandstone
682 reservoir to develop an enhanced geothermal system: Laboratory and field experiments,
683 *Geothermics*, 39(1), 70–77.
- 684 Zimmermann, G., T. Tischner, B. Legarth, and E. Huenges (2009), Pressure-dependent
685 production efficiency of an enhanced geothermal system (EGS): stimulation results and
686 implications for hydraulic fracture treatments, *Pure and applied geophysics*, 166(5),
687 1089–1106.
- 688 Zimmermann, G., I. Moeck, and G. Blöcher (2010), Cyclic waterfrac stimulation to de-
689 velop an enhanced geothermal system (EGS) - conceptual design and experimental
690 results, *Geothermics*, 39(1), 59–69.

Figure 1. Micrographs of intact andesite (A and B) and of 930°C heat-treated andesite (C and D) in Scanning Electron Microscopy. (A) General observations of the layout. Large (few mm) phenocrystals of plagioclases and pyroxenes are included in a matrix composed of smaller crystals (B). (C and D) The heat-treatment induces an dramatic increase of crack density and newly created cracks propagate in phenocrystals and in the matrix.

Figure 2. Schematic view of the experiment. A pore pressure increase from 0.2 MPa to 20 MPa is applied upstream. The downstream pump is off but can record the pore pressure. Local pore pressure measurements are recorded with fibre optics along the sample at three different positions.

Figure 3. Response of the three fibre optics to an increase of pressure from 2 MPa to 40 MPa. Fibres 1 and 3 show a linear response to applied pressure and Fibre 2 shows an hysteresis. This calibration data is used to calculate the local pore pressure as a function of the three fibres response during the pore pressure pulse propagation.

Parameter	Symbole	value
Porosity	ϕ	1.5%
Downstream volume	V_1	50 ml
Fluid bulk modulus	K_f	2.2 GPa
Rock bulk modulus	K_d	9.5 GPa
Sample radius	r	2.5 cm
Sample length	L	10 cm
Intrinsic permeability	k	10^{-18} m^2
Fluid density	ρ	1000 kg/m ³
Gravitational force	g	9.8 m/s ²
Fluid dynamic viscosity	η	$1.002 \times 10^{-3} \text{ Pa.s}$

Table 1. Summary of the parameters and their values used in the model.

Figure 4. Imposed upstream flow (blue), downstream flow (red) and mean flow (green) are plotted as a function of time during permeability measurements made during hydrostatic loading. The inset is a zoom on the three flows when upstream flow is at its minimum value (0.01ml/min).

Figure 5. (a) Evolution of the volumetric strain plotted versus confining pressure during the hydrostatic loading (in blue) and unloading (in red). The black line corresponds to a linear elastic behaviour for a static bulk modulus of 9.5 GPa. The dashed line corresponds to the crack closure pressure inferred from the volumetric strain. The microcrack porosity is shown by an arrow labelled mp in the Figure. (b) Evolution of the permeability is plotted as a function of the confining pressure during loading (blue) and unloading (red). The dashed line corresponds to the crack closure pressure inferred from (a). (c) Evolution of the permeability is plotted as a function of volumetric strain during loading (blue) and unloading (red).

Figure 6. (a) Evolution of controlled upstream (blue) and measured downstream (black) pore pressure as a function of time after application of a pressure increase from 0.2 MPa to 20 MPa upstream. Local pore pressure measurements with three fibre optics located along the sample are also shown in red, green and yellow from upstream to downstream. (b) Evolution of pore pressure across time is plotted as a function of length along the sample. (c) Zoom on the 20 minutes at the beginning of the experiment (grey shaded area in (a)). (d) Same as (b) for the 20 minutes at the beginning of the experiment. (e) Zoom on the 10 minutes at the beginning of the experiment (grey shaded area in (a)). (f) Same as (b) and (d) for the 10 first minutes of the experiment.

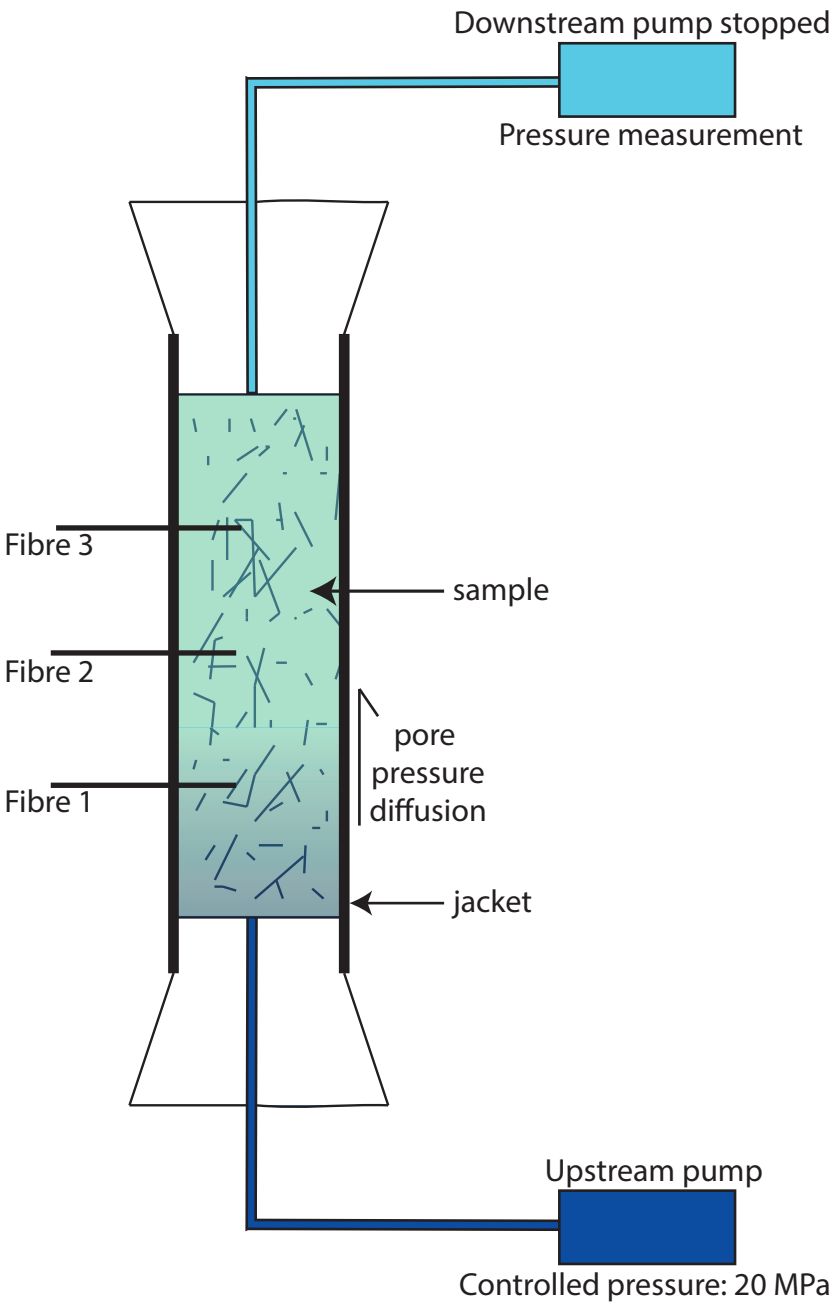
Figure 7. (a) Evolution of differential stress and volumetric strain as a function of time during triaxial loading. (b) Evolution of volumetric (red) and axial (green) strains as a function of time under constant triaxial stress before pressure pulse propagation.

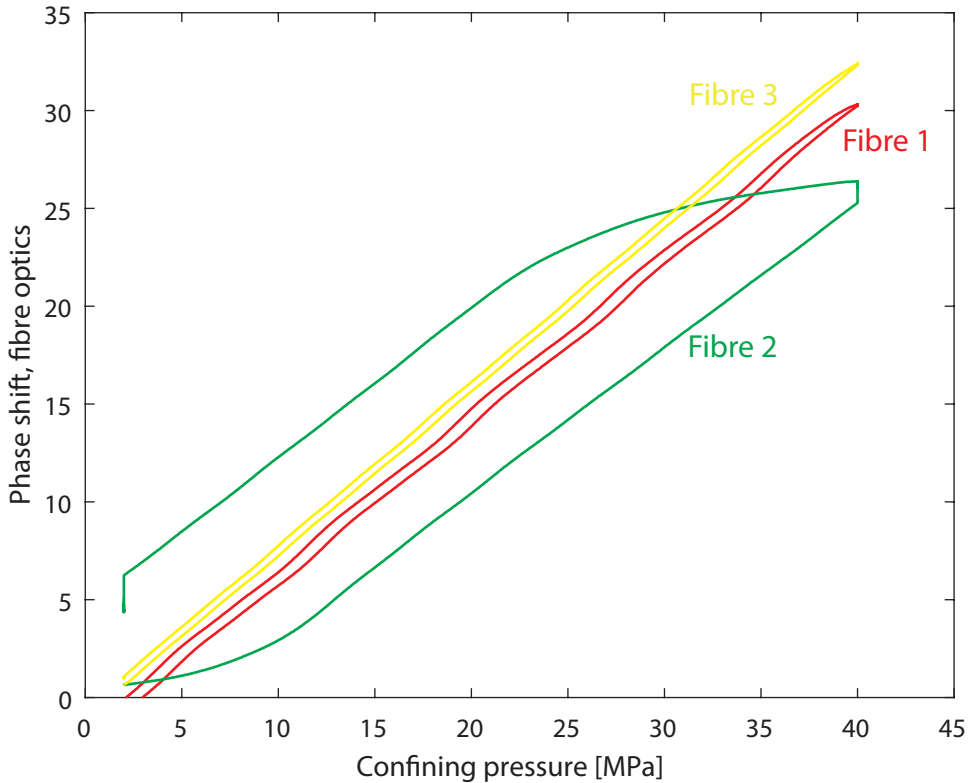
Figure 8. (a) Evolution of controlled upstream (blue) and measured downstream (black) pore pressure as a function of time after application of a pressure increase from 0.2 MPa to 35 MPa upstream at a confining pressure of 40 MPa and a differential stress of 356 MPa. Local pore pressure measurements with three fibre optics located along the sample are shown in red, green and yellow from upstream to downstream. (b) Evolution of pore pressure across time is plotted as a function of length along the sample for the pressure pulse sent under a confining pressure of 40 MPa and a differential stress of 356 MPa.

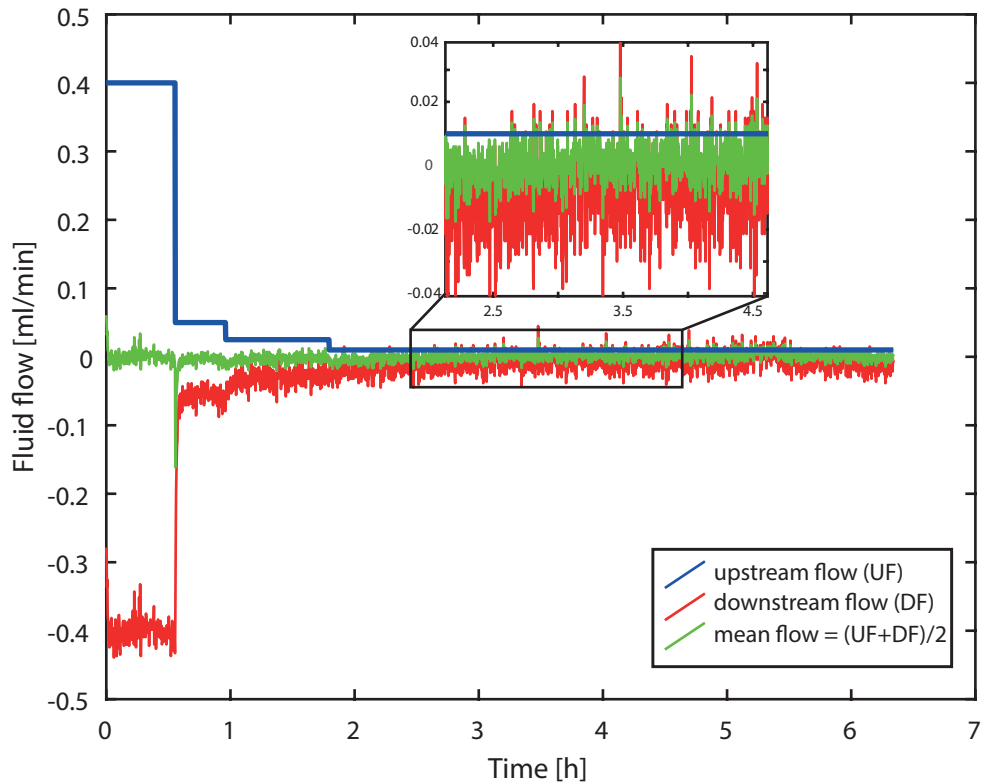
Figure 9. (a) Evolution of controlled upstream (blue) and measured downstream (black) pore pressure as a function of time after application of a pressure increase from 0.2 MPa to 20 MPa upstream under a hydrostatic stress state. Local pore pressure measurements with three fibre optics located along the sample are also shown in red, green and yellow from upstream to downstream. Red, green and yellow dots correspond to pore pressure along the sample calculated with Darcy's law using upstream and downstream pressure for the positions of the three fibre optics of corresponding color. (b) Same as (a) zooming on the 10 minutes at the beginning of the experiment (grey shaded area in (a)). (c) Evolution of permeability as a function of time calculated between two following pressure measurements made either with the microvolumetric pumps or the fibre optics. Light blue curve corresponds to the permeability calculated between upstream and downstream pumps with Darcy's law.

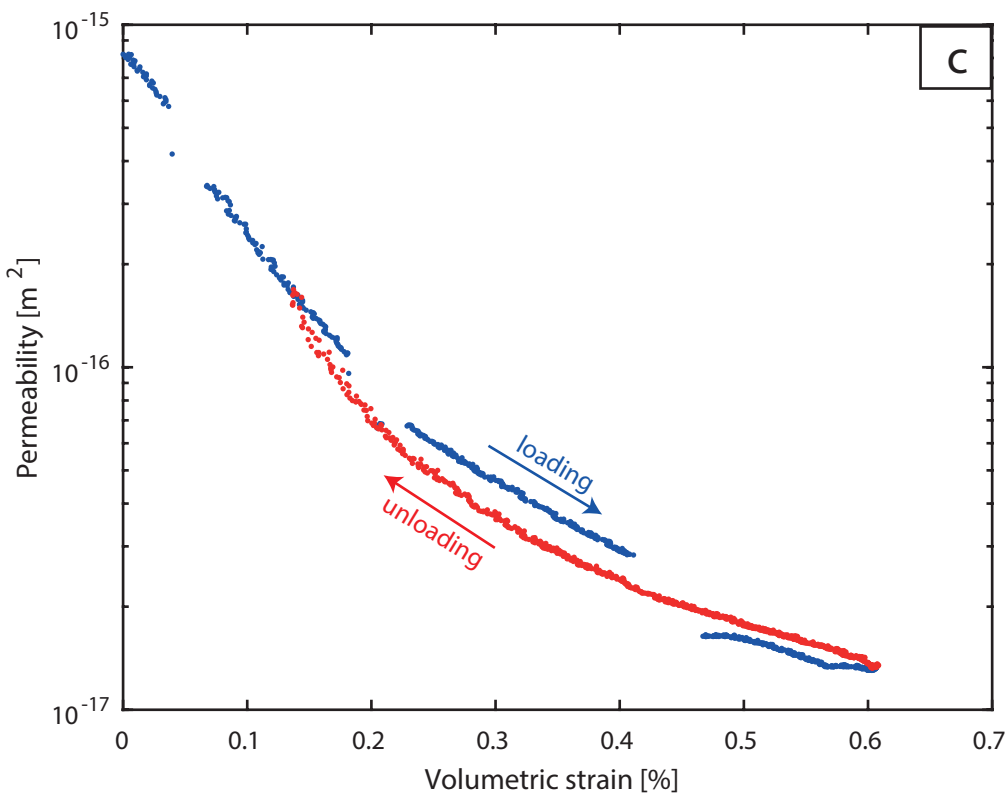
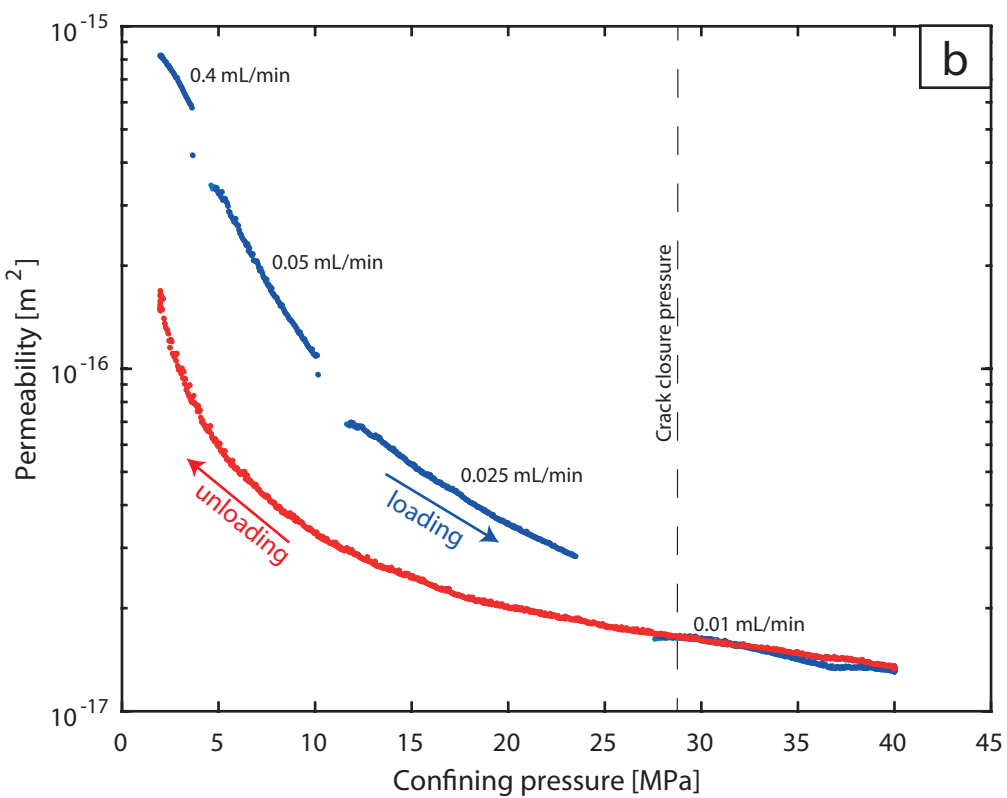
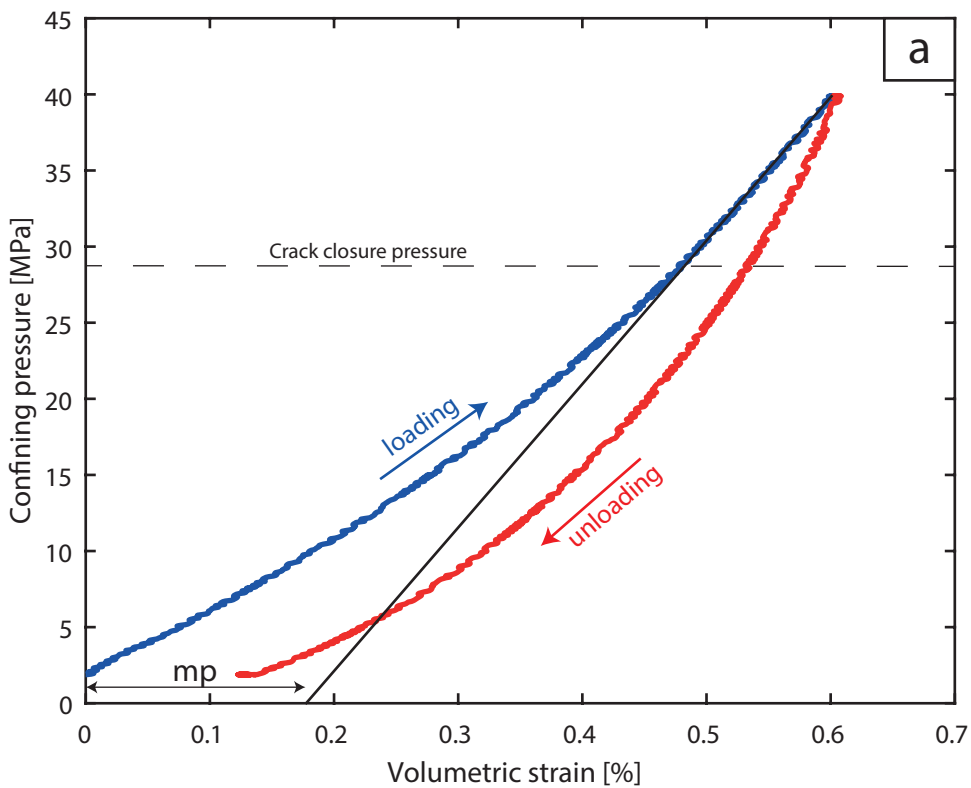
Figure 10. Schematic view of the model. We consider the diffusion of pore fluid through a porous medium (rock sample) into the downstream dead volume composed of the tubing and the Quizix pump.

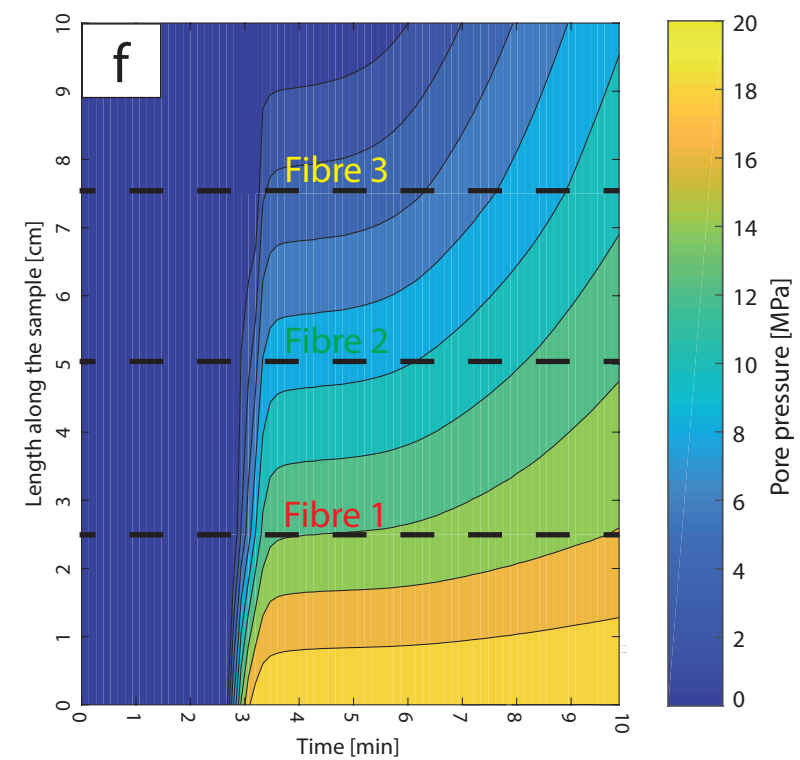
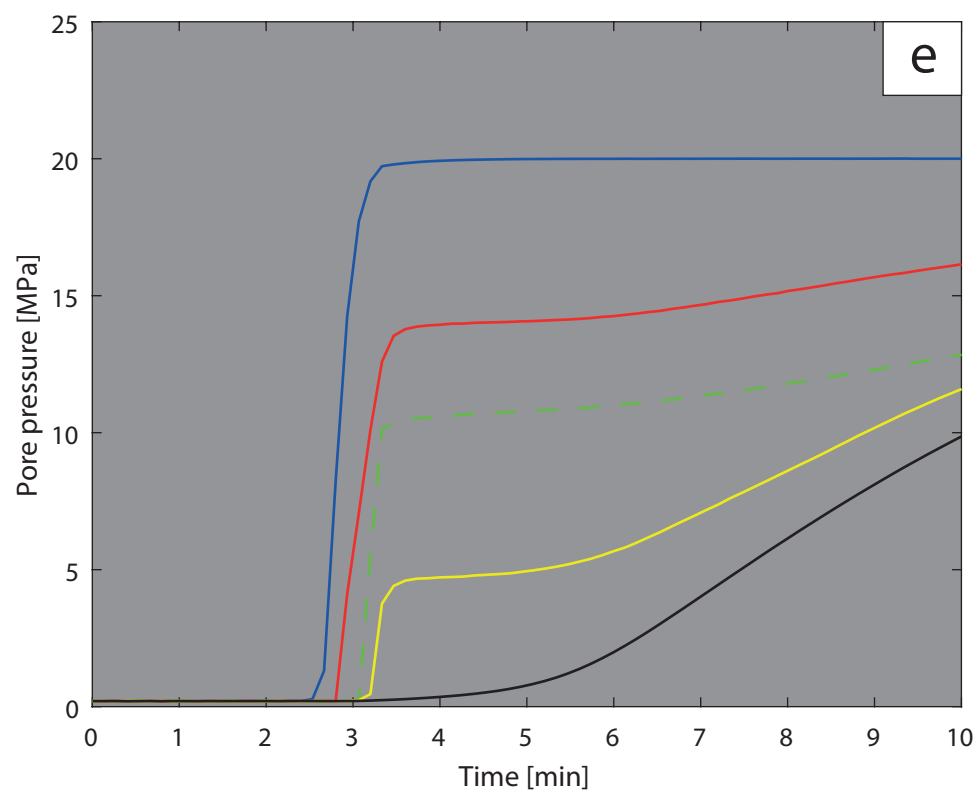
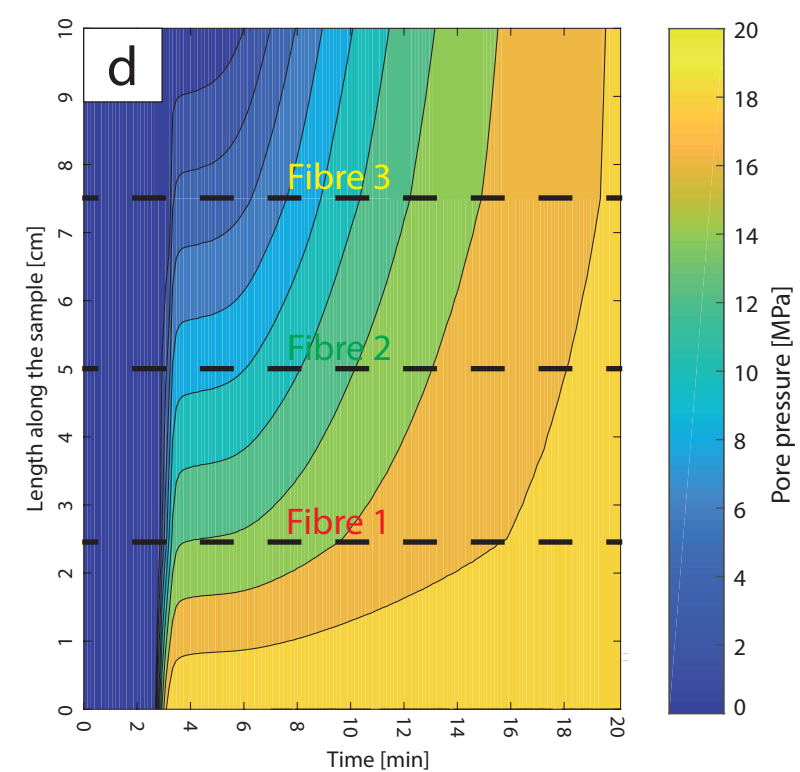
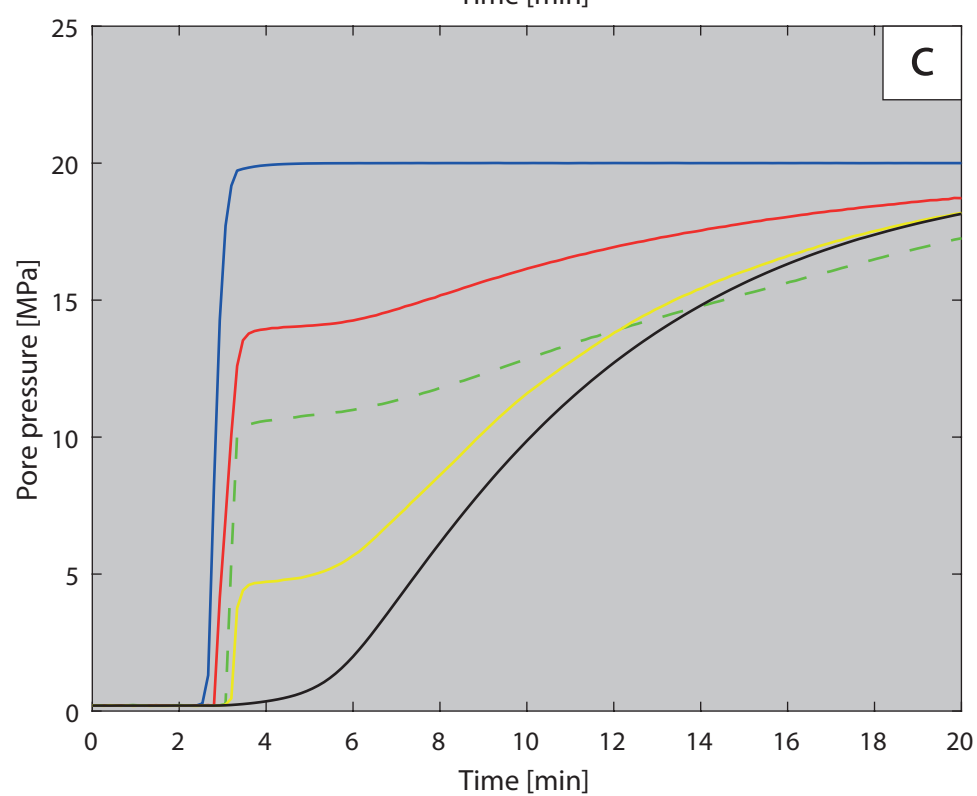
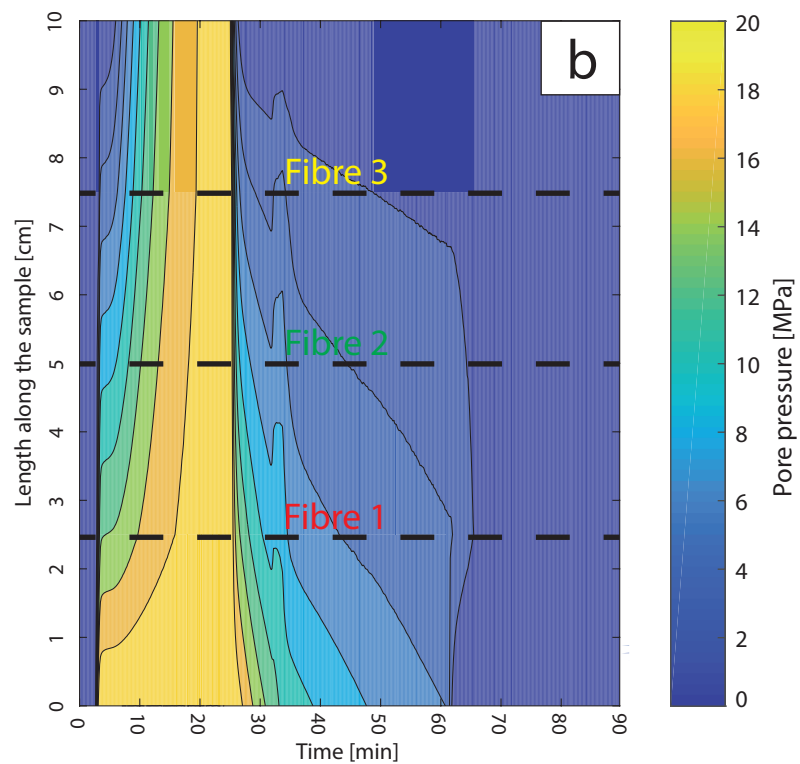
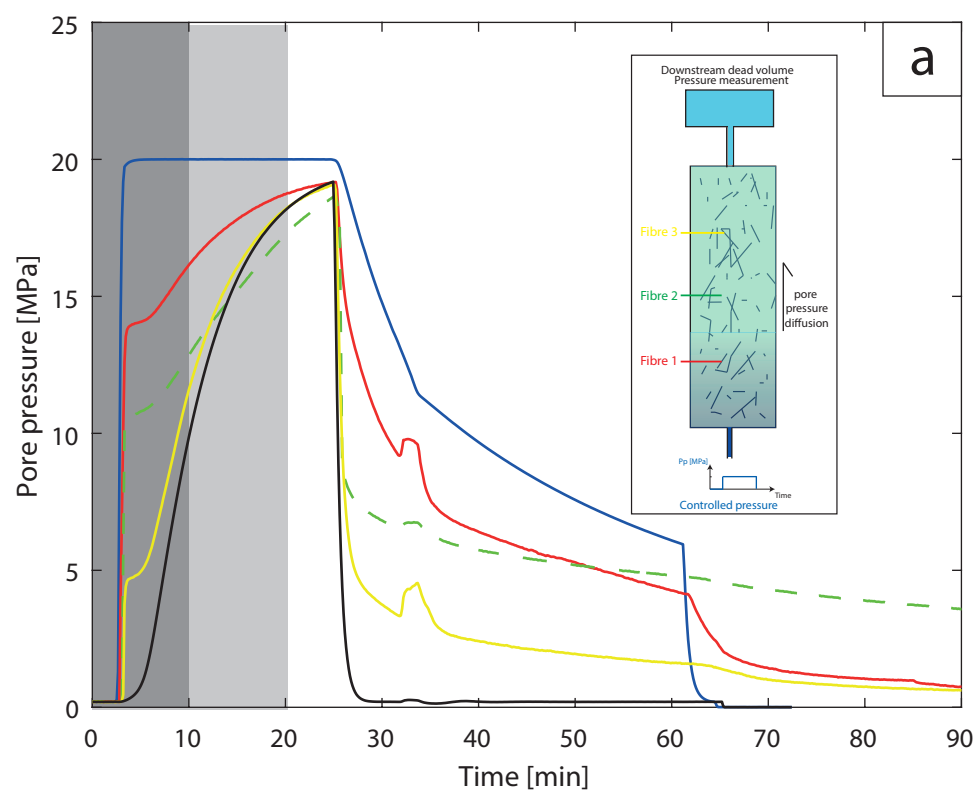
Figure 11. Comparison of data and results of the model for pressure measurements upstream, downstream and along the sample for a pore pressure pulse sent under a hydrostatic pressure of 40 MPa.

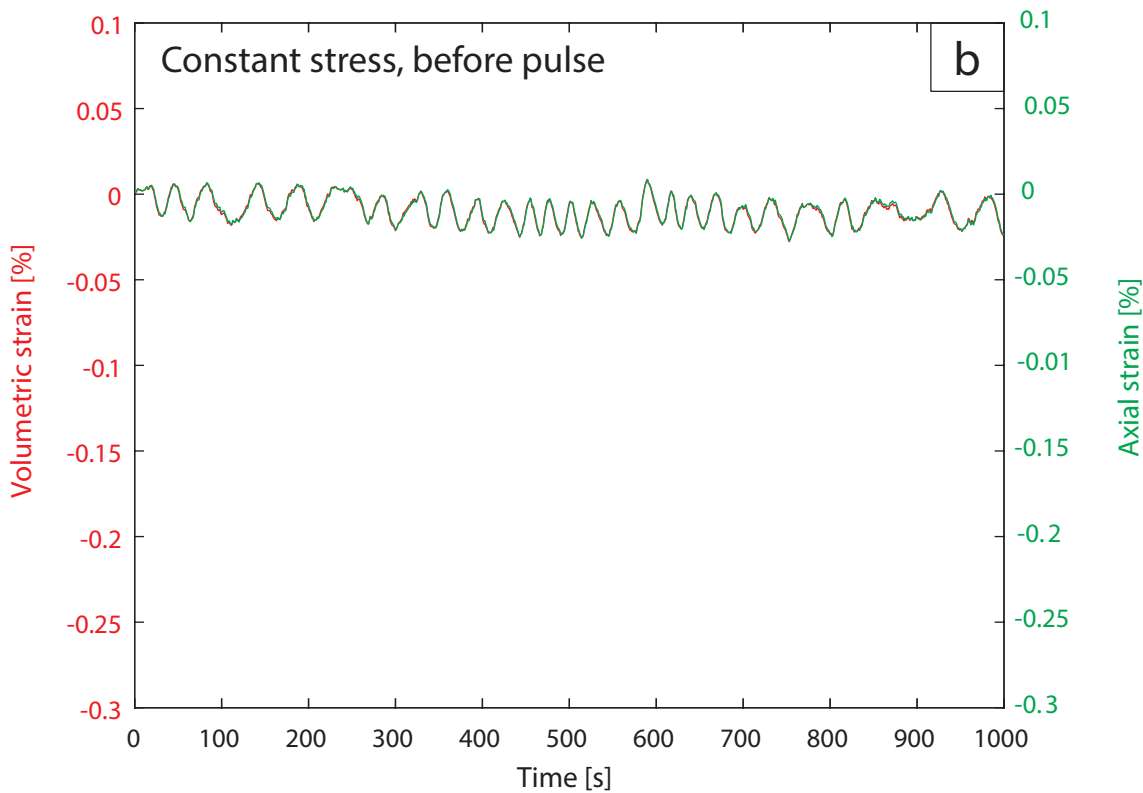
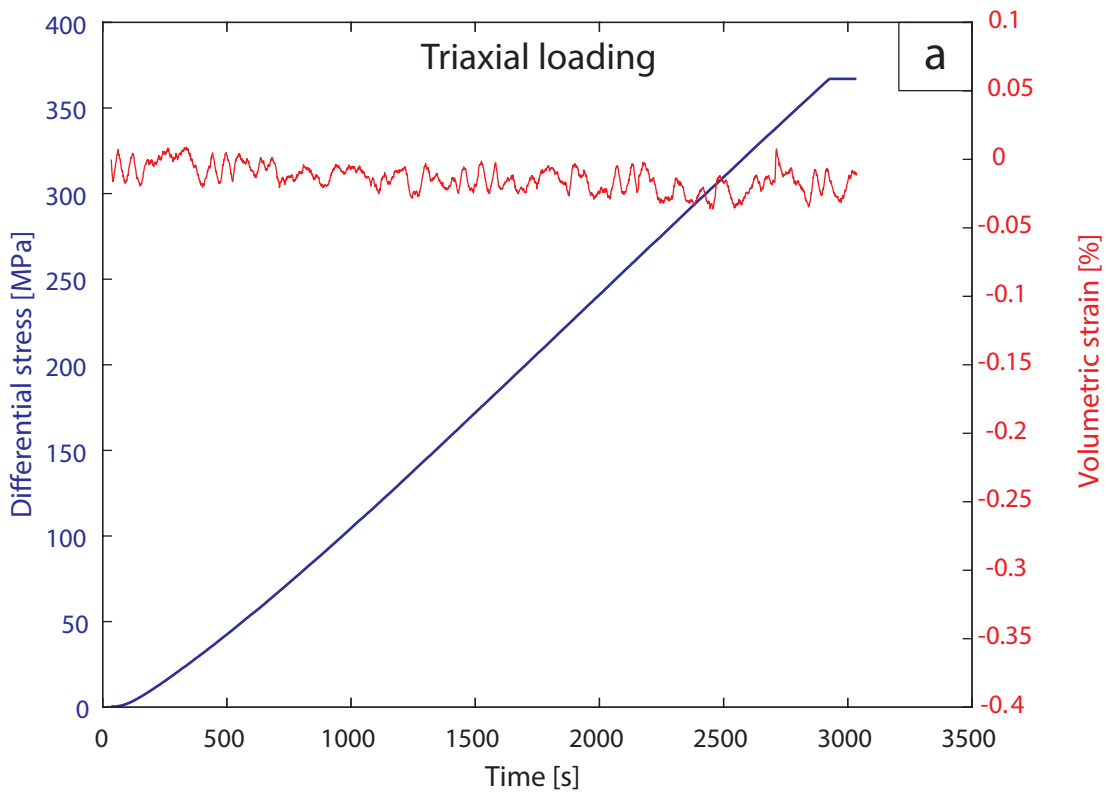


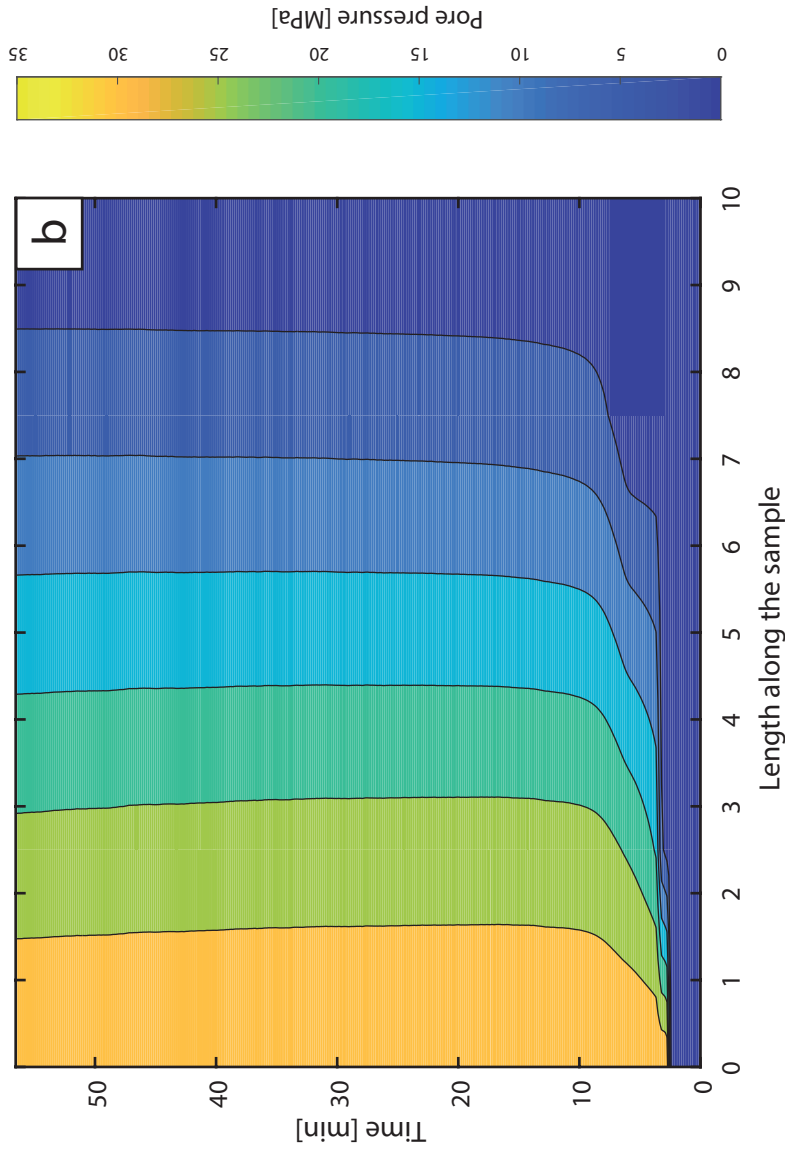
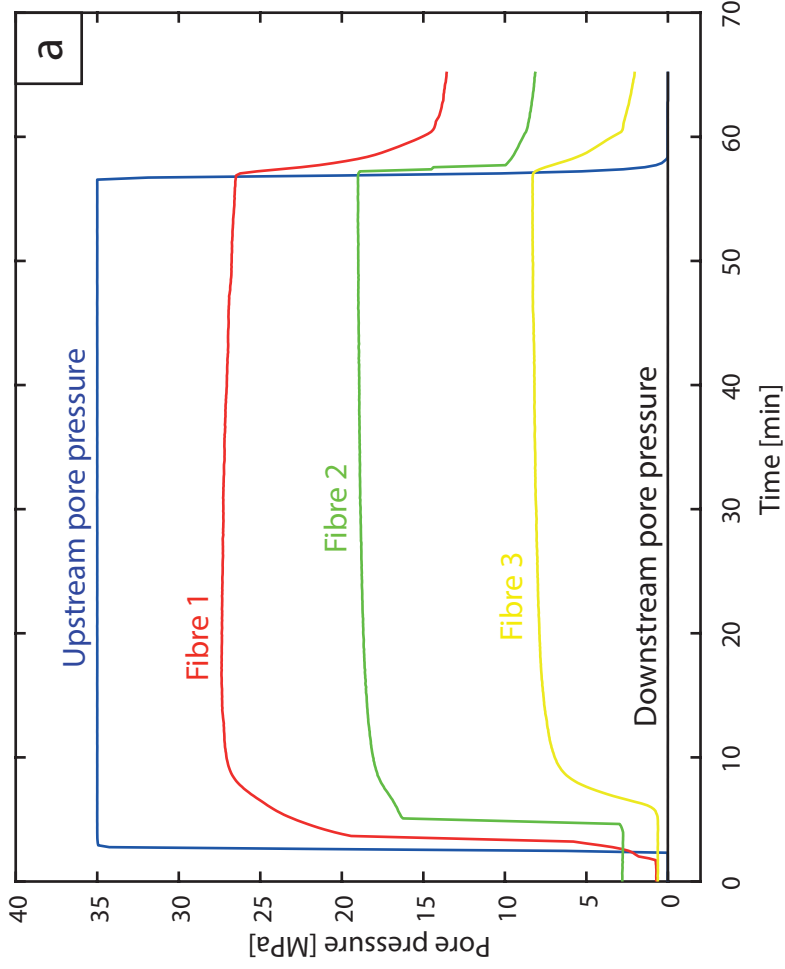
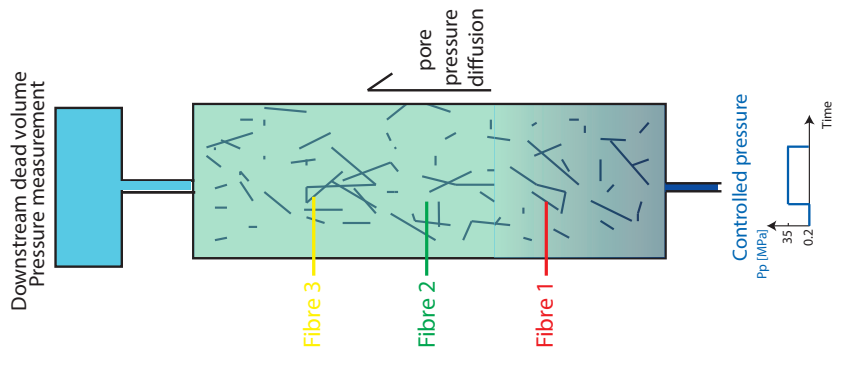


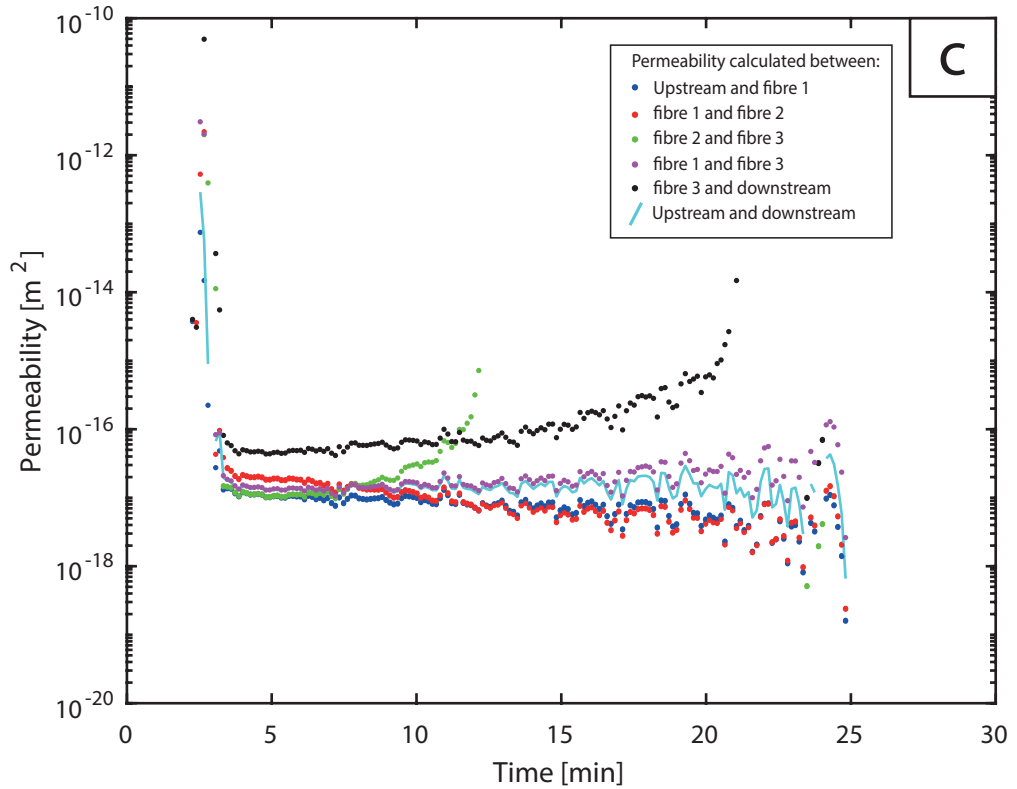
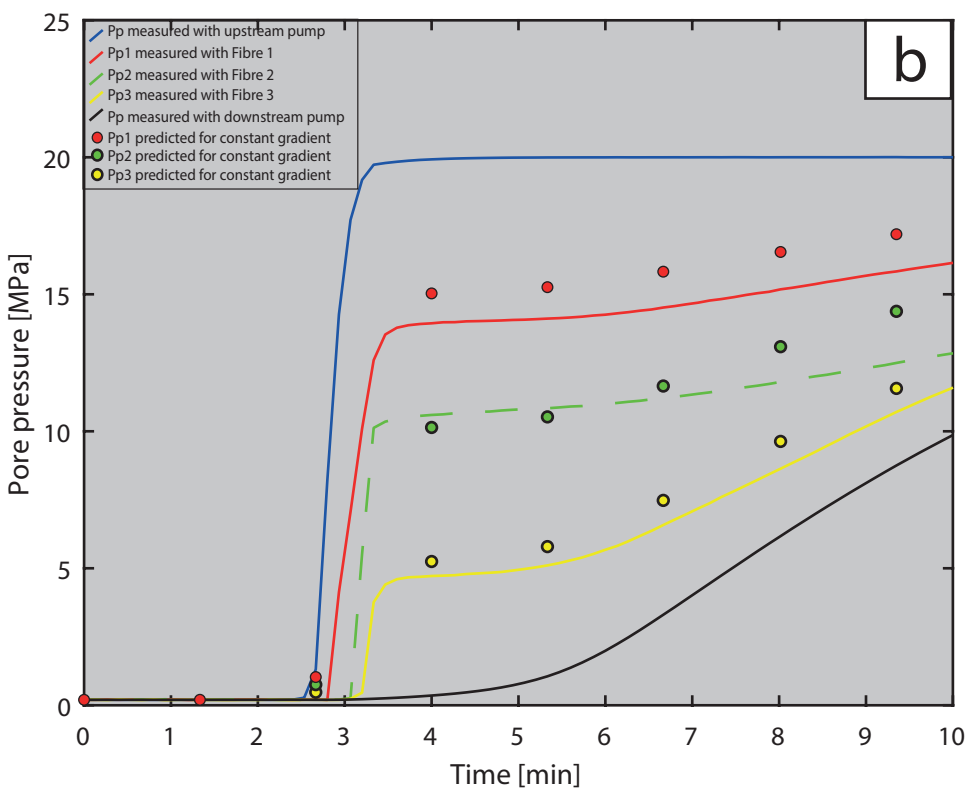
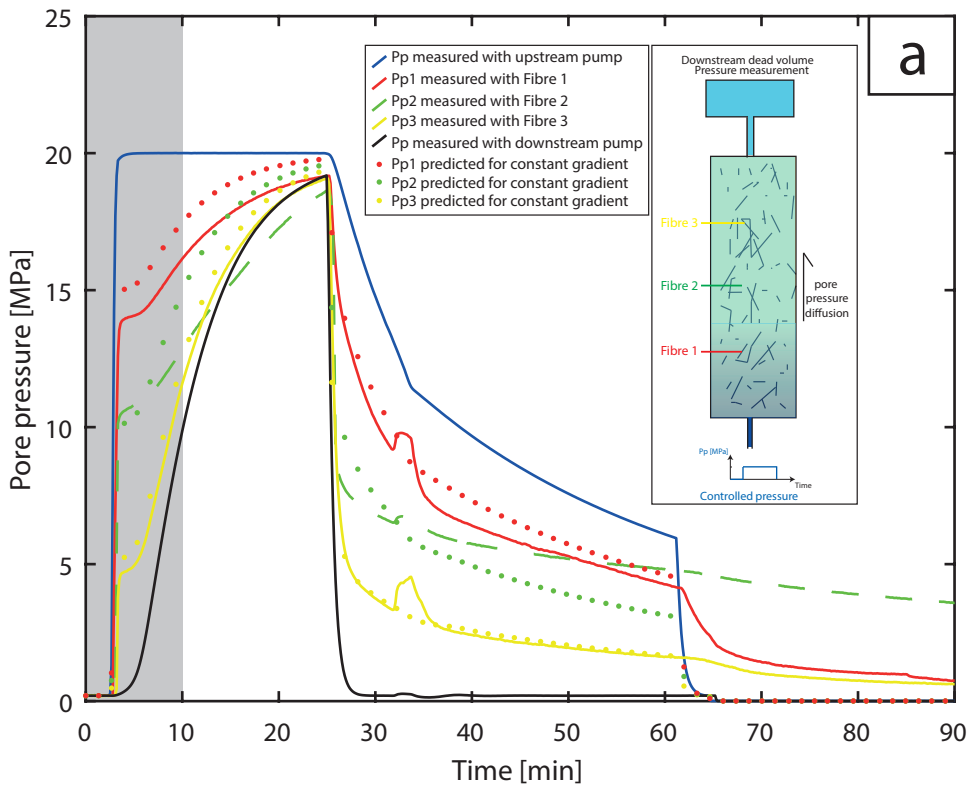




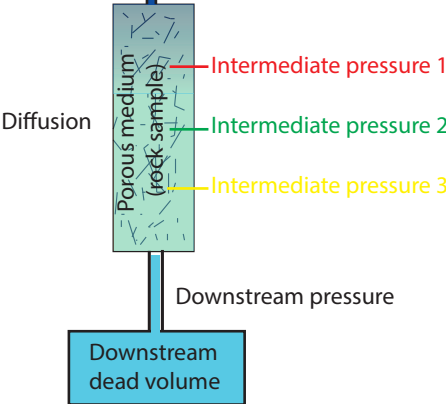








Controlled pressure



Porous medium
(rock sample)

Intermediate pressure 1

Intermediate pressure 2

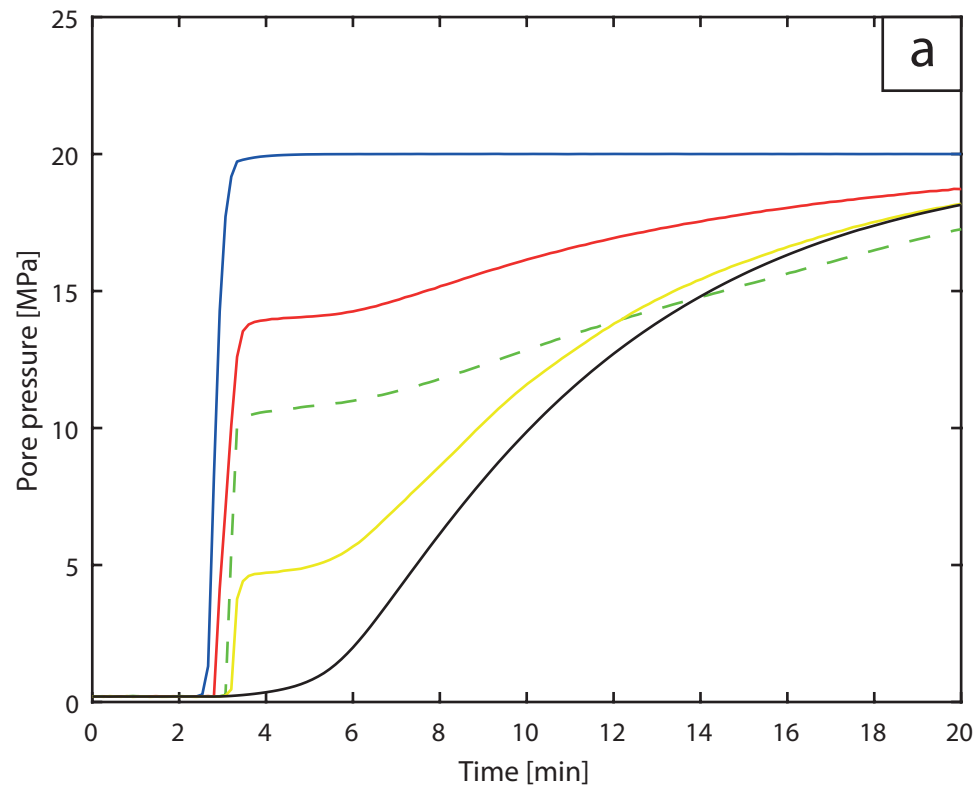
Intermediate pressure 3

Diffusion

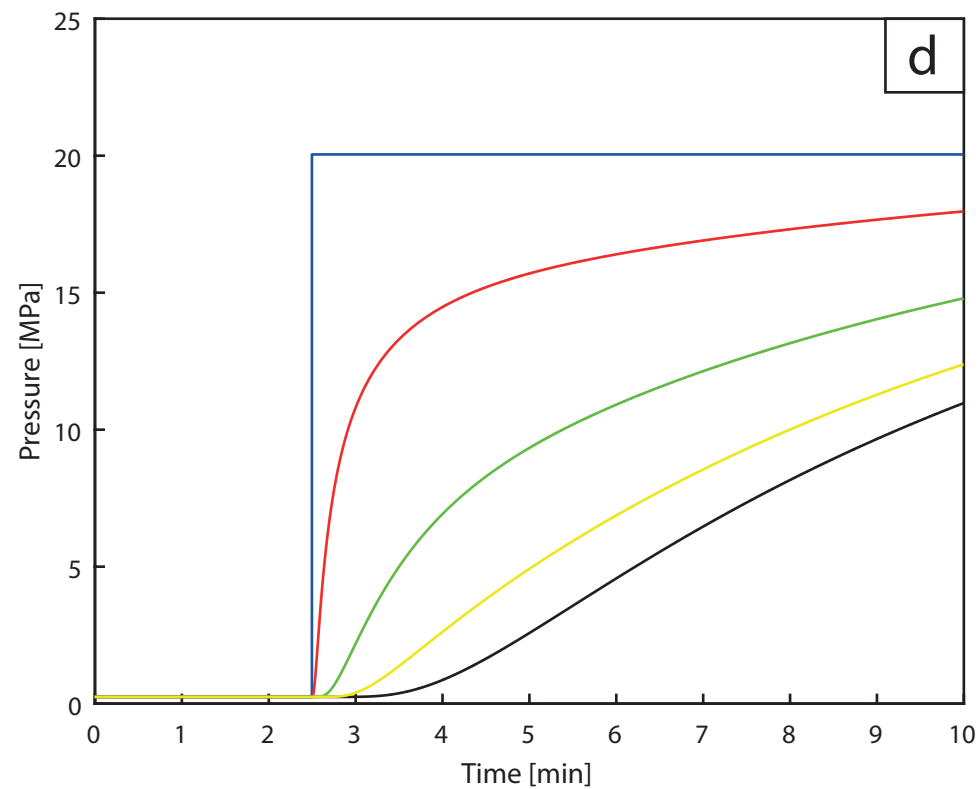
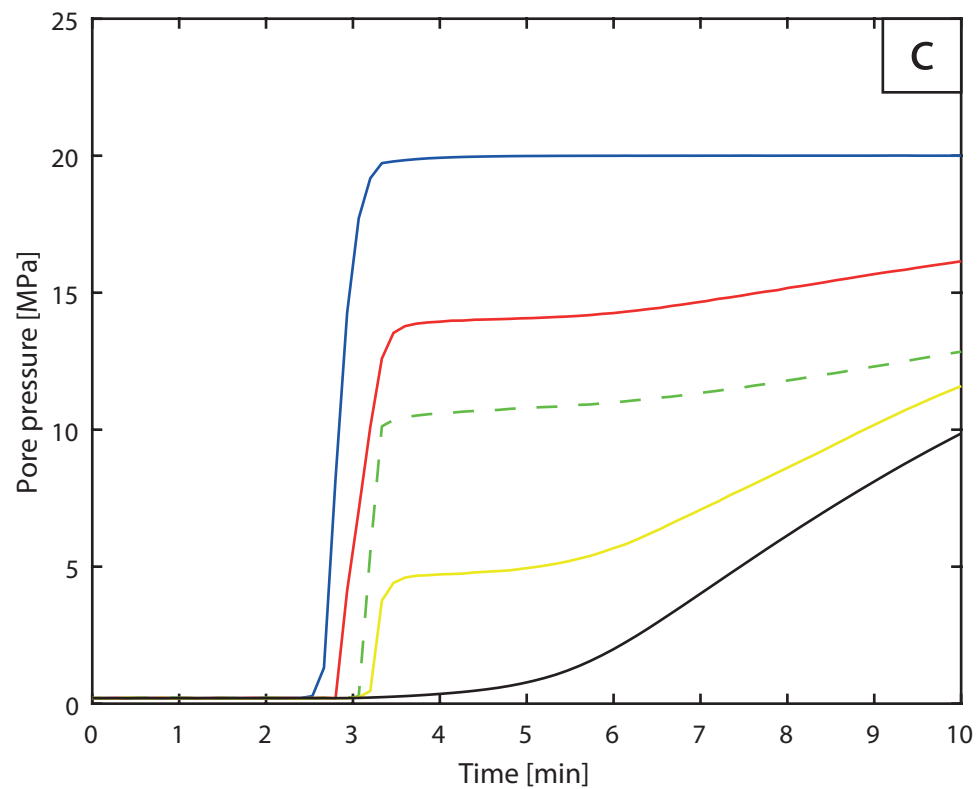
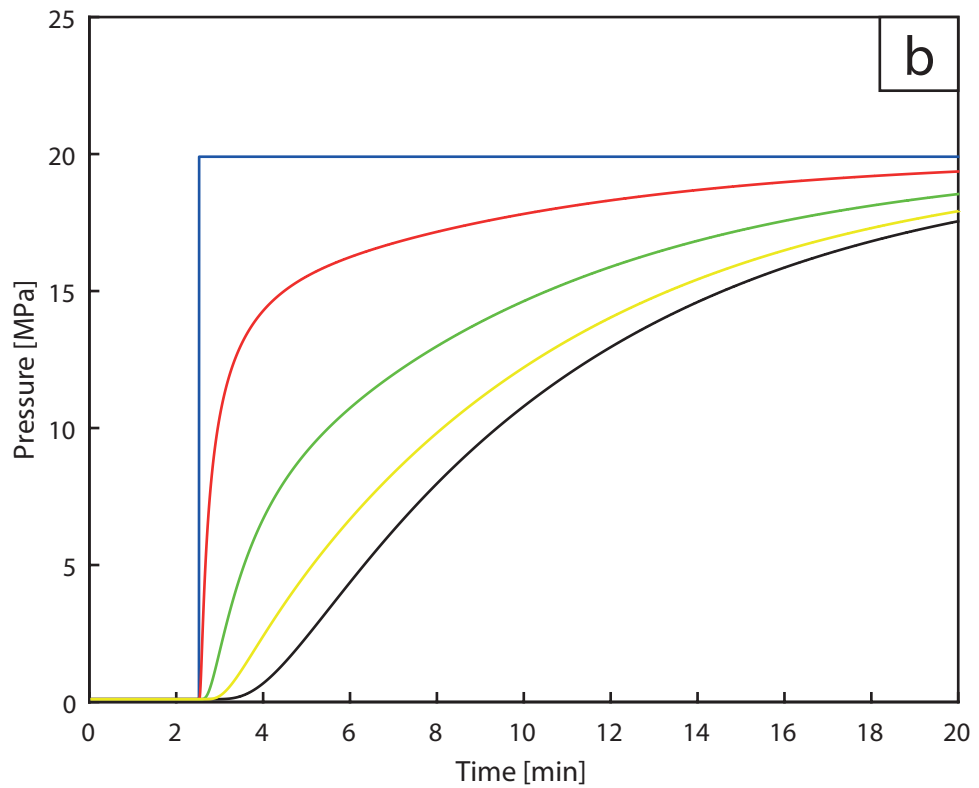
Downstream pressure

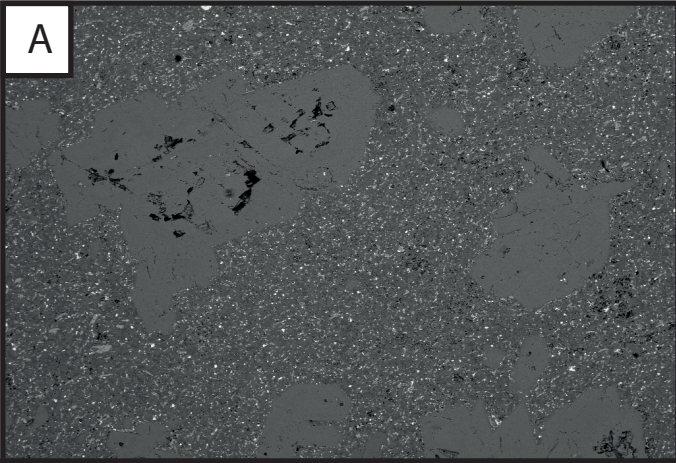
Downstream
dead volume

DATA

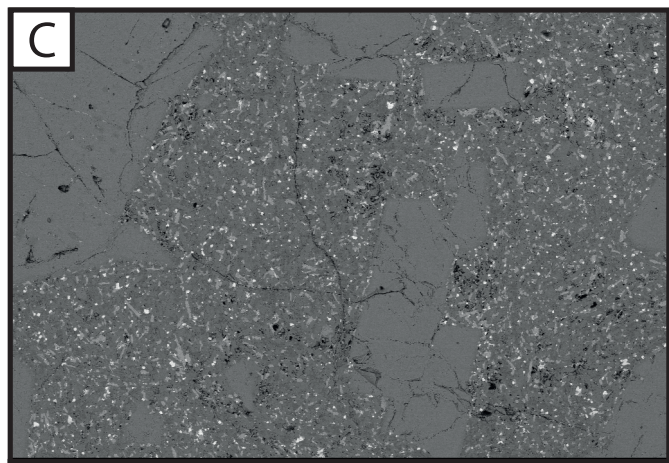


MODEL

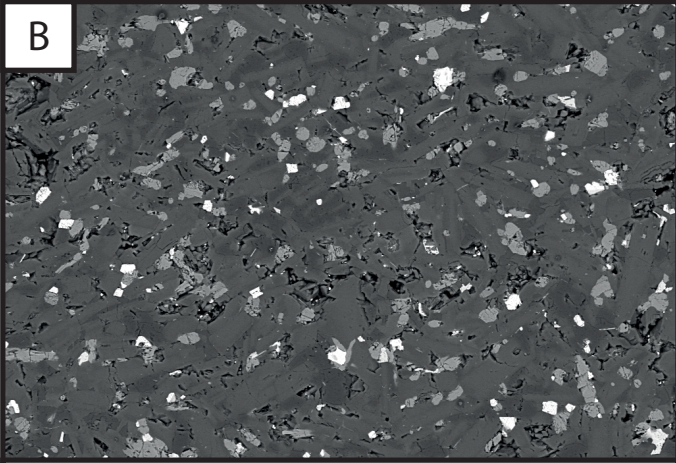


A200 μm

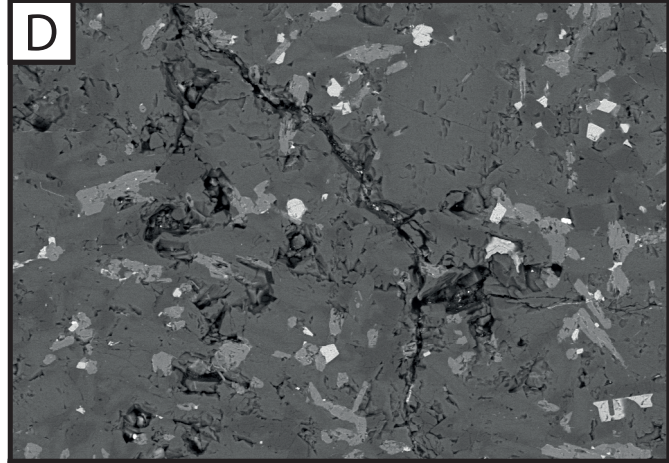
EHT=15kV

C200 μm

EHT=15kV

B20 μm

EHT=15kV

D20 μm

EHT=15kV